The Astrophysical Journal, 941:11 (21pp), 2022 December 10 https://doi.org/10.3847/1538-4357/ac9964
© 2022. The Author(s). Published by the American Astronomical Society.
OPEN ACCESS

Ultra-diffuse Galaxies as Extreme Star-forming Environments. I. Mapping Star Formation in H I-rich UDGs

Erin Kado-Fong[1], Jenny E. Greene[1], Song Huang[2], and Andy Goulding[1]
[1] Department of Astrophysical Sciences, Princeton University, Princeton, NJ 08544, USA; kadofong@princeton.edu
[2] Department of Astronomy, Tsinghua University, Beijing 100084, People's Republic of China
Received 2022 May 20; revised 2022 October 2; accepted 2022 October 5; published 2022 December 7

Abstract

Ultra-diffuse galaxies (UDGs) are both extreme products of galaxy evolution and extreme environments in which to test our understanding of star formation. In this work, we contrast the spatially resolved star formation activity of a sample of 22 H I-selected UDGs and 35 low-mass galaxies from the NASA Sloan Atlas (NSA) catalog within 120 Mpc. We employ a new joint spectral energy distribution fitting method to compute star formation rate and stellar mass surface density maps that leverage the high spatial resolution optical imaging data of the Hyper Suprime-Cam Subaru Strategic Program and the UV coverage of the Galaxy Evolution Explorer, along with H I radial profiles estimated from a subset of galaxies that have spatially resolved H I maps. We find that UDGs have low star formation efficiencies as a function of their atomic gas down to scales of 500 pc. We additionally find that the stellar mass-weighted sizes of our UDG sample are unremarkable when considered as a function of their H I mass—their stellar sizes are comparable to NSA dwarfs at fixed H I mass. This is a natural result in the picture where UDGs are forming stars normally, but at low efficiencies. We compare our results to predictions from contemporary models of galaxy formation, and find in particular that our observations are difficult to reproduce in models where UDGs undergo stellar expansion due to vigorous star formation feedback should bursty star formation be required down to $z = 0$.

Unified Astronomy Thesaurus concepts: Dwarf galaxies (416); Low surface brightness galaxies (940); Star formation (1569); Extragalactic astronomy (506)

Supporting material: machine-readable table

1. Introduction

Ultra-diffuse galaxies (UDGs) are dwarf galaxies that are characterized by large stellar sizes ($R_{\rm eff} > 1.5$ kpc) and low surface brightnesses ($\mu_{0,g} > 24$ mag arcsec^{-2}, though exact definitions vary; see Van Nest et al. 2022 for an overview). These diffuse systems are extreme in two senses: they lie far above the mass–size relation, making them extreme products of galaxy evolution, but they are also extreme environments for star formation due to their low stellar surface densities.

UDGs as extreme products of galaxy evolution is a well-trodden topic both observationally (see, e.g., Sandage & Binggeli 1984; McGaugh et al. 1995; Dalcanton et al. 1997; van Dokkum et al. 2015; Beasley & Trujillo 2016; Peng & Lim 2016; Yagi et al. 2016; Leisman et al. 2017; van Dokkum et al. 2018; Danieli et al. 2019; Janowiecki et al. 2019; van Dokkum et al. 2019; Danieli et al. 2021; Gault et al. 2021) and theoretically (e.g., Amorisco & Loeb 2016; Di Cintio et al. 2017; Greco et al. 2018a, 2018b; Chan et al. 2018; Jiang et al. 2019; Liao et al. 2019; Wright et al. 2021; Van Nest et al. 2022; Zaritsky et al. 2022). However, the formation of the UDG population remains an open question. Several mechanisms have been proposed to form UDGs in the field, including stellar expansion from star formation feedback (El-Badry et al. 2016; Di Cintio et al. 2017; Chan et al. 2018), early mergers that trigger radial expansion of star formation (Wright et al. 2021), and preferential UDG formation in the high spin tail of the halo distribution (Dalcanton et al. 1997; Liao et al. 2019).

It is observationally challenging to measure robust distances to UDGs due to their low surface brightnesses; as a result, the majority of UDGs with known distances are in clusters or groups. To understand the full breadth of the UDG population, of course, it is necessary to sample this population across a range of environments. Observational works continue to place new constraints on such mechanisms (see, e.g., Leisman et al. 2017; Greco et al. 2018a, 2018b; Janowiecki et al. 2019; Martín-Navarro et al. 2019; Gault et al. 2021; Kado-Fong et al. 2021; Greene et al. 2022; Villaume et al. 2022), but as of yet there has not been a clear convergence in the literature toward one path—of course, it is also not necessarily the case that all UDGs are formed via the same mechanism. Toward this end, there has been a push to use H I to detect and/or measure distances to UDGs (Leisman et al. 2017; Janowiecki et al. 2019; Karunakaran et al. 2020; Gault et al. 2021) — this allows for distance determinations in a sample of UDGs that tend toward low-density environments.

It has been shown that although H I-selected UDGs lie on the star-forming main sequence (SFMS) and the H I mass–size relation (Gault et al. 2021), they tend to have high H I masses (Leisman et al. 2017)—that is, UDGs are, in an integrated sense, low in their star formation efficiency as a function of atomic gas, or SFE(H I). This in and of itself is not surprising—it has been demonstrated observationally that stellar mass surface density affects the position of dwarf galaxies with respect to the Kennicutt–Schmidt relation (Schmidt 1959; Kennicutt 1989) in that lower stellar mass surface density dwarfs lie below the main relation (de los Reyes & Kennicutt 2019). What has not yet been ascertained, however, is whether the apparently low SFE(H I) of

Original content from this work may be used under the terms of the Creative Commons Attribution 4.0 licence. Any further distribution of this work must maintain attribution to the author(s) and the title of the work, journal citation and DOI.

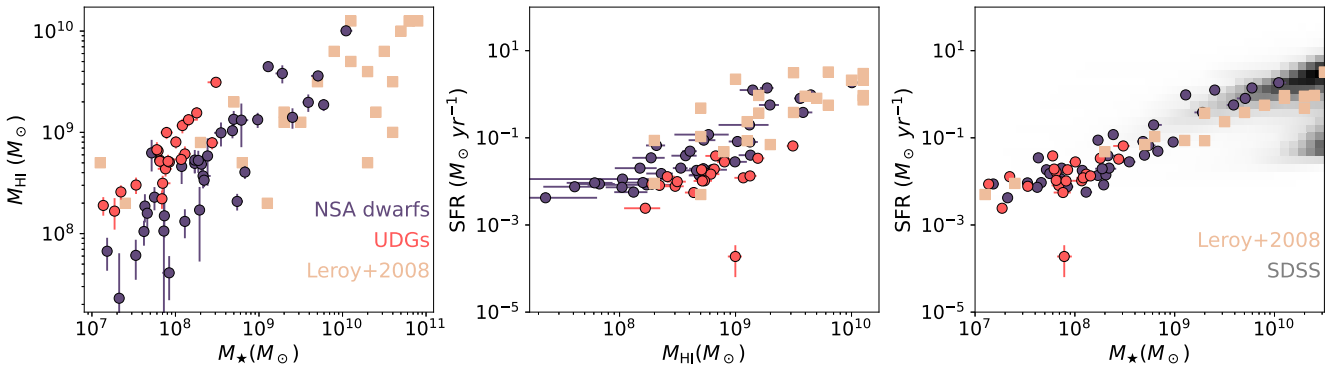

Figure 1. A comparison of the integrated properties of the samples derived in this work against the directly measured result of Leroy et al. (2008; beige points). In all panels, the red points show UDGs and the purple points show NSA dwarfs. From the left, we show the relationship between stellar mass and H I mass, the relationship between H I mass and SFR, and the SFMS. In the SFMS panel, we also show the results of the SDSS DR7 MPA-JHU value-added catalogs in grayscale (Kauffmann et al. 2003; Brinchmann et al. 2004; Salim et al. 2007). We find a good agreement between our results and those from the literature. Although UDGs have high H I masses for their stellar mass (left panel), they have relatively little SFR for their H I mass (middle panel).

UDGs is a product of their selection, the distribution of their star formation, or a true physical suppression of SFE(H I).

In order to understand the origin of the low SFE(H I) of UDGs, we introduce a joint spectral energy distribution (SED) fitting method that utilizes the spatial resolution of the optical Hyper Suprime-Cam Subaru Strategic Program (HSC-SSP) and the crucial UV coverage of the Galaxy Evolution Explorer (GALEX). We use this method to derive stellar mass and star formation rate (SFR) maps of a sample of H I-selected UDGs from Janowiecki et al. (2019) and a reference sample of H I-detected galaxies from the NASA Sloan Atlas (NSA; Bradford et al. 2015). We then use these maps, along with estimated H I radial profiles, to probe the star formation efficiency of these dwarfs down to 500 pc scales. In this work, our main focus is characterizing the properties of the H I-selected UDGs with respect to the *normal* NSA dwarf sample through a lens aimed largely at galaxy evolution. In Kado-Fong et al. (2022, hereafter Paper II) we will shift our focus toward understanding star formation in H I-rich UDGs, with a particular focus on the role of UDG structure in the pressure-regulated, feedback-modulated model of star formation (Ostriker et al. 2010; Kim et al. 2011; Ostriker & Shetty 2011; Kim et al. 2013; Kim & Ostriker 2015; Kim et al. 2017).

2. Data Sets

Our dwarf sample consists of two main branches: a high surface brightness, normal dwarf sample drawn from the H I catalog of Bradford et al. (2015)—hereafter the NSA sample, and a UDG sample with known distances from the H I catalog of Janowiecki et al. (2019). The UDG sample is selected to have a maximum distance of $d = 120$ Mpc; we enforce the same limit on the NSA sample. We note that in this work we will refer to the normal galaxy sample as the NSA sample, as these galaxies were not specifically chosen to exclude low surface brightness galaxies. Rather, their relatively high surface brightnesses are a result of the observational selection that leads to their inclusion in the NSA.

2.1. Sample Overview

Here, we detail the basic physical properties of the UDG and NSA samples. The sample consists of 58 galaxies at distances less than 120 Mpc; 22 are UDGs from Janowiecki et al. (2019) and 35 are NSA galaxies from Bradford et al. (2015). All sources are required to have clean five-band HSC imaging, and all sources have measured H I masses and redshifts due to their selection method. The sample of Janowiecki et al. (2019) is not explicitly chosen to be in the field (in contrast to Leisman et al. 2017), but they find that the properties of their H I-selected UDGs are largely unchanged by the environment. We find that one UDG in our sample, AGC 227965, is quenched (SFR $< 10^{-3}\,M_\odot\,\mathrm{yr}^{-1}$), due to being a close satellite of Mrk 1324. We leave this galaxy in our analysis as it still yields a significant H I detection, but note that our discussion of the field UDG formation pathways does not apply to this system.

In Figure 1, we show our sample galaxies in stellar mass versus H I mass (left), SFR versus H I mass (center), and the SFMS (right). These results are from a customized SED fitting method that we describe in detail in Section 3, but can be thought of as standard SED fitting results for the purposes of the figures in this section. In this figure and all subsequent figures, we show the NSA sample in purple and the UDG sample in red. The NSA sample reaches higher stellar masses and lower H I masses than does the UDG sample; when noted, we only compare NSA galaxies with stellar masses within the observed range of the UDG sample. The results of the Leroy et al. (2008) sample of nearby galaxies and the Sloan Digital Sky Survey (SDSS) spectroscopic value-added catalog (Kauffmann et al. 2003; Brinchmann et al. 2004; Salim et al. 2007) are shown in beige and gray, respectively. We see that the UDGs have high H I masses for their stellar masses and that they have low SFRs for their H I masses—conversely, the UDGs lie directly on the SFMS.

A clear question arises from this initial analysis: are the H I-selected UDGs truly drawn from a more H I-rich population than the NSA dwarfs, or are the higher H I masses simply an effect of observational selection? To test this, we consider what our expected distribution of UDG H I fractions, $f_{\mathrm{H\,I}} = M_{\mathrm{H\,I}}/(M_\star + M_{\mathrm{H\,I}})$, would be given the 21 cm flux limit of the UDG sample if the $f_{\mathrm{H\,I}}$ distribution of the UDGs were the same as that of the NSA sample. To put it another way, we ask the following question: if the UDG population had the same distribution of H I fractions as the NSA dwarf sample, what is the distribution of $f_{\mathrm{H\,I}}$ that one would expect to see from an H I-selected sample?

We show the results of this test in Figure 2. The top panel shows the observed 21 cm line fluxes in solid points (as always, purple for the NSA sample and red for UDGs), while the unfilled red points show the expected 21 cm flux for each UDG in the

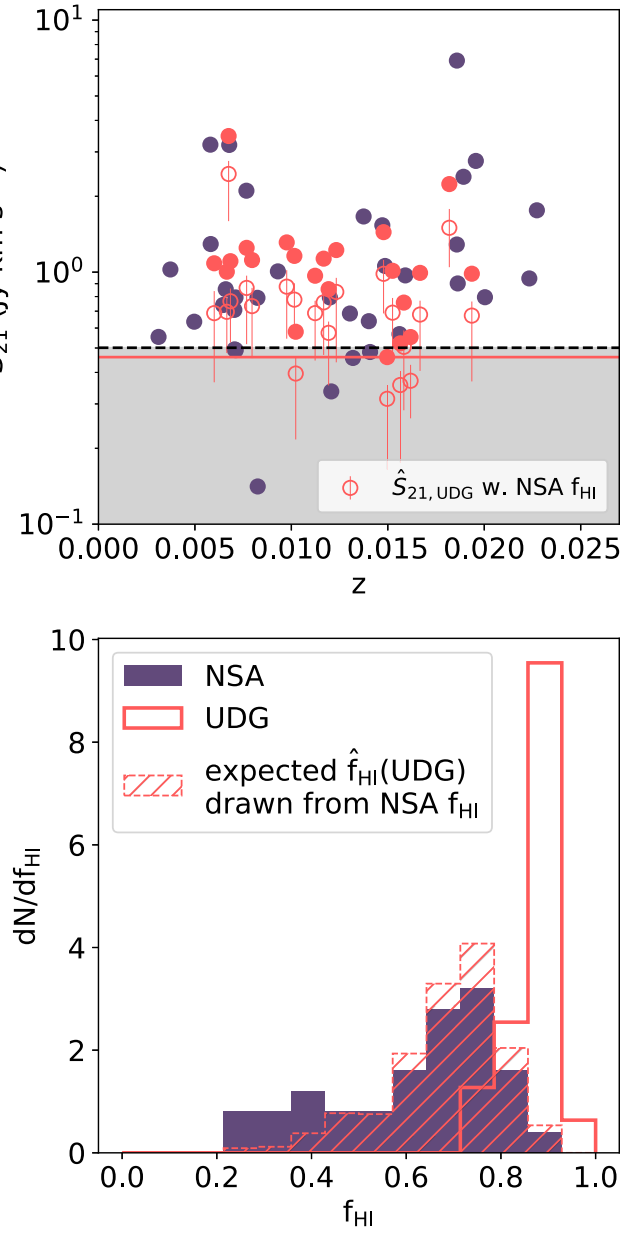

Figure 2. Top: 21 cm line flux (S_{21}) vs. redshift for the NSA (purple) and UDG (red) samples. The nominal ALFALFA flux limit is shown by the dashed black line, while the minimum S_{21} of the UDG sample is shown in red. The unfilled symbols show the expected S_{21} of each of the galaxies in the UDG sample if we assume that the distribution over the H I fraction of the underlying UDG population is identical to that of NSA dwarfs. Bottom: the distribution over observed H I fractions for the NSA (filled purple histogram) and UDG (unfilled red histogram) samples. The hatched red histogram shows the distribution of H I fractions that we would expect to see from the UDG sample if the distribution over H I fractions is identical between the UDG population and NSA sample. We thus conclude that the UDG sample is inconsistent with having the same distribution over $f_{\mathrm{H\,I}}$ as the NSA sample.

sample if the H I fraction were drawn from the NSA dwarf distribution over $f_{\mathrm{H\,I}}$. The error bars in this panel are generated via bootstrap resampling from the NSA distribution. We estimate the detection limit of the UDG sample in two ways: first, from the stated completeness limit of the ALFALFA survey for sources with $1.65 < \log_{10}(W_{50}/[\mathrm{km\ s^{-1}}]) < 1.7$ (Haynes et al. 2011, black dashed line), and second, from the lowest 21 cm flux of the UDG sample (red solid line). These limits are in good agreement with one another, and we adopt the minimum 21 cm line flux of the UDG sample as our detection limit for this exercise. The bottom panel of Figure 2 shows the distribution of observed H I fractions for the NSA (solid purple histogram) and UDG (unfilled red histogram) samples, as well as the UDG sample that we would expect to have detected if the UDG distribution over $f_{\mathrm{H\,I}}$ were the same as that of the NSA sample (hatched dashed red histogram). Indeed, we find that we would expect to detect a significant number of $f_{\mathrm{H\,I}} \lesssim 0.75$ UDGs, should they exist. Rather, the marked H I richness of the UDG sample cannot simply be attributed to observational limits.

We extend this positioning of H I-rich UDGs as unusual star-forming environments by considering a globally averaged stellar mass, H I, and SFR surface density as shown in Figure 3. In this figure, we compute $\Sigma_{\mathrm{H\ I,\ global}}$ using the total H I mass and the total area (as defined by the global elliptical HSC-g aperture, which we will describe in Section 3). One can immediately see that, as expected from their definition, UDGs have significantly lower SFR and stellar mass surface densities than the NSA sample. Intriguingly, however, UDGs do *not* also show signs of lower H I surface densities. Indeed, their H I surface densities span the same range as their spectroscopic counterparts.

The main thrust of this paper will be to root out the physical culprits of this apparently lowered SFE(H I). From globally averaged measurements alone, it is unclear whether the low average SFR surface density is a result of a truly lower SFE (H I), or whether the spatial distribution of star formation in UDGs differs from normal dwarfs (e.g., a low globally averaged Σ_{SFR} could arise from an old stellar population that is significantly more extended than the star-forming regions). In order to distinguish between these two scenarios, we must build an SED fitting method to constrain local (500 pc scale) SFR and stellar mass surface densities (Section 3)—we will return to this narrative of star formation efficiency in Section 5.

2.2. UV-optical Imaging

HSC-SSP. The HSC-SSP imaging boasts wide spatial coverage, high sensitivity (a point-source depth of $i_{\mathrm{HSC}} \sim 26$ in its shallowest *wide* layer), and high spatial resolution (the worst-seeing band, g_{HSC}, has an average seeing of $0\farcs77$).

For this work, we use the internal data release S21A, which covers 670 deg^2 in five optical bands. The HSC-SSP data products include two options for the background subtraction—a local subtraction suited for small, high redshift sources, and a global subtraction suited for nearby galaxies. We use the coadd/bg versions of the co-added HSC images, which use the *global* background subtraction of the S18A and PDR2 data releases (for an in-depth discussion of the HSC global background subtraction scheme, see Section 4.1 of Aihara et al. 2019 and Li et al. 2022). The data have been shown to reach surface brightness limits of $i_{\mathrm{HSC}} \sim 28.5$ mag arcsec^{-2} for radially averaged measurements around a known target (Huang et al. 2018; Kado-Fong et al. 2020).

GALEX. To complement the deep and high-resolution optical imaging of the HSC imaging, we draw upon archival GALEX imaging to measure the global UV photometry of our galaxies. We use the package astroquery to query the Barbara A. Mikulski Archive for Space Telescopes (MAST) for GALEX far-UV (FUV) and near-UV (NUV) observations that cover the position of each galaxy. We adopt the average GALEX point-spread functions (PSFs) in this work; the FUV and NUV PSFs have an FWHM of $4\farcs2$ and $4\farcs9$, respectively.[3]

[3] http://www.galex.caltech.edu/researcher/techdoc-ch5.html

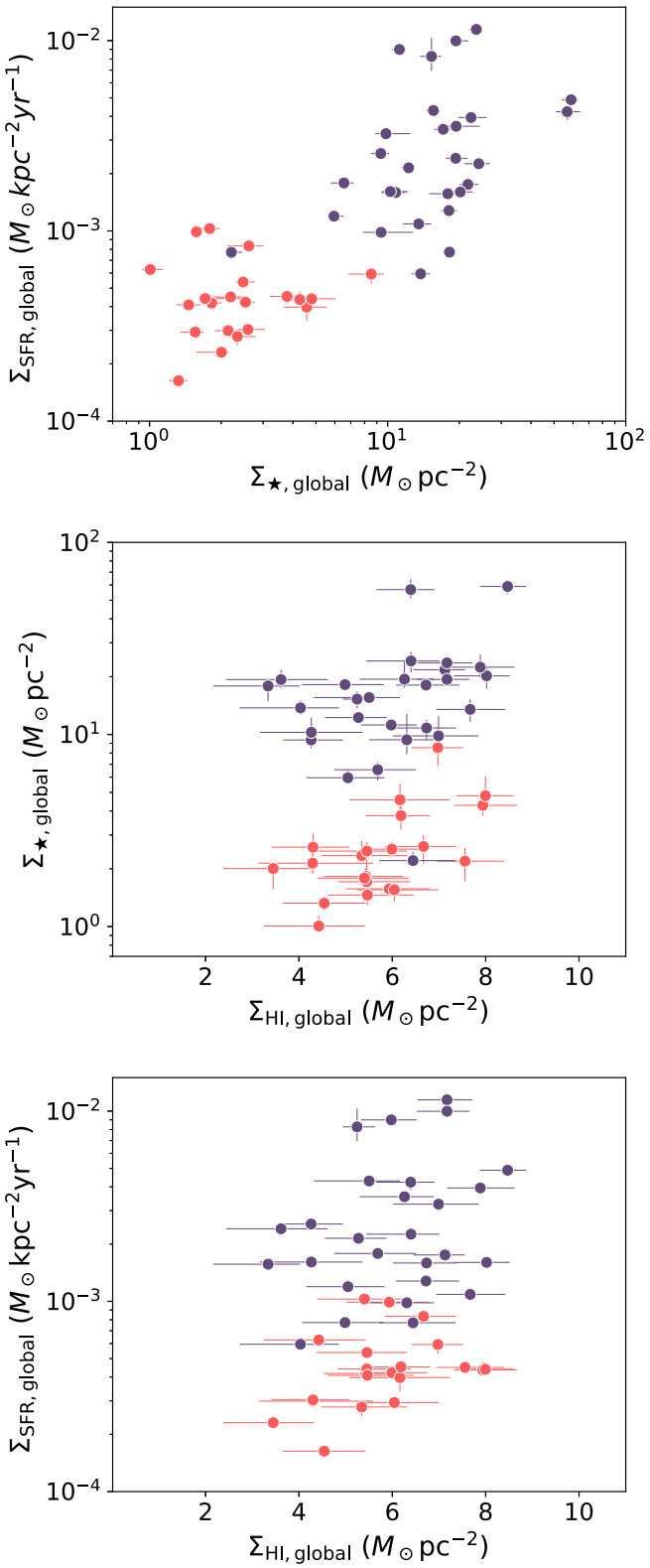

Figure 3. Estimates of the SFR, stellar mass, and H I surface densities in a globally averaged sense, i.e., the ratio between the integrated measurement and the isophotal size of the galaxy. UDGs are shown in red and NSA dwarfs in purple for all cases. In this figure, we exclude all NSA dwarfs with stellar masses exceeding $M_\star = 10^9 M_\odot$.

We measure our GALEX photometry on the background-subtracted intensity maps provided by the GALEX pipeline, and estimate uncertainties assuming Poisson noise for the counts.

For targets with more than one GALEX archival image, we prefer the data product with a longer total exposure time. Two NSA galaxies (NSA ID 5109 and 30738) do not have FUV imaging; all galaxies have NUV imaging. Of our sample with FUV imaging, 13 galaxies are drawn from the GALEX All-Sky Imaging Survey (AIS; $m_{AB} = 20.5$) and 35 from the Medium Imaging Survey (MIS; $m_{AB} = 23.5$, Martin et al. 2005). 13 are drawn from guest investigator (GI) programs; we make an estimate of the depth of the GI programs by measuring the standard deviation of random apertures of apertures the size of the average GALEX FWHM. The GI imaging is somewhat deeper than the MIS imaging, with a mean 5σ depth of $m_{AB} = 24.3$. Similarly, six galaxies in our sample have NUV AIS imaging, 40 have MIS imaging, and nine have GI imaging. We repeat the same procedure to estimate the depth of the GI imaging and find a mean 5σ depth of $m_{AB} = 23.4$. We note that the depths estimated here are not used in the analysis, and are simply meant to contextualize the GALEX imaging sources for the reader.

2.3. H I Measurements

All of the galaxies in the present work have integrated H I measurements from Janowiecki et al. (2019, UDGs) or Bradford et al. (2015, NSA galaxies). However, resolved H I measurements exist only for a small subset of the UDGs identified by Janowiecki et al. (2019)—12 from Gault et al. (2021) and three from Leisman et al. (2017).

To estimate the radial profiles of the H I in our UDG and NSA dwarf samples, we leverage the empirical result that UDGs and normal dwarfs are similar in their H I structure—that is, UDGs lie on the H I mass–size relation and have typical average H I surface densities (Gault et al. 2021). We use this result to estimate Sérsic profile parameters for our sample via a parameter estimation from the spatially resolved measurements of Hunter et al. (2021; who report Sérsic parameter fits for their sample), as well as the spatially resolved measurements of the UDGs in Gault et al. (2021).[4] We perform a least squares fit to the Sérsic index, n, central surface density, $\Sigma_{0,H\,I}$ and effective radius, $R_{eff,H\,I}$, of the literature samples as a function of H I mass; only $R_{eff,H\,I}$ shows a significant correlation with H I mass (i.e., the H I mass–size relation). This allows us to estimate Sérsic parameters for our galaxies as a function of their H I mass. As these structural measures are not well constrained, we will account for the uncertainties induced by our estimated H I profiles to demonstrate to the reader that these estimates are indeed reasonable.

First, although the Sérsic profile has three free parameters, our knowledge of the total H I mass allows us to determine the value of one of these parameters given estimates for the other two. We therefore choose to fix the H I central surface density via the analytic solution for the total H I mass of a 1D Sérsic profile, i.e.,

$$M_{H\,I} = 2\pi \int_0^\infty \Sigma_{H\,I}(R) R dR$$
$$= 2\pi\Sigma_0 n \left(\left(\frac{1}{h}\right)^{1/n}\right)^{-2n} \Gamma(2n). \quad (1)$$

We find that the Σ_0 values derived from a fit to the literature data and the Σ_0 values derived using the total H I mass are in good agreement, with the latter method resulting in Σ_0 values that are on average ~8% higher than the former.

[4] Here, we solve for the Sérsic parameters of their galaxies using the given measures of the H I structure.

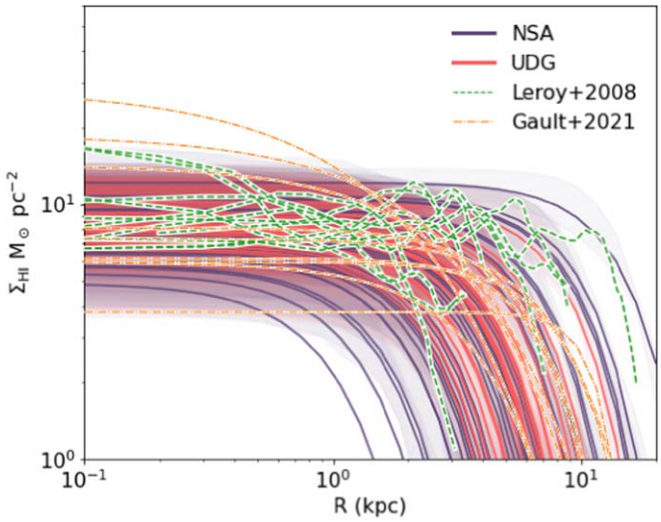

Figure 4. A comparison between our estimates of the H I surface density radial profiles for the UDG (red solid curves) and NSA (purple solid curves) samples against spatially resolved H I measurements of dwarfs from the literature. We show the direct radial profiles of Leroy et al. (2008) in green, and Sérsic fits inferred for a sample of H I-rich UDGs from the H I spatial distribution metrics provided by Gault et al. (2021) in orange. We find that our radial profile estimates are in good agreement with these direct literature measurements.

Second, to account for the substantial uncertainty induced by our lack of spatially resolved H I, we include an uncertainty in the parameter estimation of the Sérsic profiles equivalent to the standard deviation of the literature parameter values for reference (literature) galaxies within 0.5 dex of that of the target (NSA/UDG) galaxy in total H I mass. If no galaxies are sufficiently close in H I mass, we increase the tolerance from 0.5 dex to up to 0.9 dex, but note that because the reference sample of Hunter et al. (2021) is systematically lower mass than our sample, this only affects the most massive ($\log_{10} M_{\rm H\,I} > 10$) galaxies in our sample. We then estimate the uncertainty on the radial H I surface density profile via Monte Carlo resampling assuming that the uncertainties are well described by normal distributions.

The resulting H I surface density profiles are shown in Figure 4; as above, red curves indicate UDGs and purple curves indicate NSA galaxies. The shaded regions span the 16th–84th percentiles of the Monte Carlo simulation result for each galaxy. The directly measured H I profiles of Leroy et al. (2008) are shown in green, while the Sérsic profiles inferred from the structural measurements of Gault et al. (2021) are shown in orange. We find that our inferred profiles are in good agreement with the shape, normalization, and scatter of the directly measured profiles, with the exception of one UDG (AGC 238764, which is not a part of our sample) that has an anomalously high Sérsic index ($n = 1.98$; almost all dwarfs in this mass range are characterized with sub-exponential Sérsic indices, see Hunter et al. 2021). There is, to our knowledge, only one H I-rich UDG that has spatially resolved H I data at a high enough resolution to probe the clumpiness and substructure of the H I (Mancera Piña et al. 2022). These data, which have a physical beam size of ∼2.9 kpc, show a significant H I substructure that is not captured in our simple radial profile estimation approach. However, the deviations from the radial profile that these azimuthal variations cause are comparable to the uncertainty we have already attributed to our radial profiles (see the right panel of Figure 1 in Mancera Piña et al. 2022). We thus find it unlikely that we are overestimating the precision of the H I profiles, though we of course note that obtaining high-resolution H I maps would dramatically improve the precision and accuracy of our $\Sigma_{\rm H\,I}$ estimates.

3. SED Fitting

The key technical challenge of this work is inferring the star formation and stellar mass properties of the dwarf sample at sub-galactic scales. We accomplish this by modeling the high spatial resolution HSC optical data in conjunction with the UV GALEX measurements to constrain star formation activity in a consistent way with the UV data.

The novelty of our approach is to leverage both the high spatial resolution of HSC and the expanded wavelength coverage of GALEX to infer local star formation surface density properties of our dwarfs via a joint fit to localized optical photometry and global UV photometry. Here, we detail the fitting process employed in this work.

3.1. Stellar Population Models

We use the Flexible Stellar Population Synthesis models (Conroy et al. 2009; Conroy & Gunn 2010) with a fixed stellar and gas-phase metallicity of $Z = 0.004$ along with a Kroupa (2001) initial mass function to generate our synthetic spectra. We choose a single value for the model metallicity as the mass–metallicity relation is not well-understood for these dwarf samples. Direct (T_e) measurements of nearby dwarfs (Lee et al. 2006; Berg et al. 2012; Jimmy et al. 2015) can show significant offsets relative to each other and to metallicity estimates from SED fitting to more distant dwarf samples (Bellstedt et al. 2021). We thus choose to adopt a typical value following the literature compilation of Bellstedt et al. (2021) for a galaxy of $M_\star \sim 10^8 M_\odot$. We also check the impact of adopting solar metallicity models in Appendix B, and find that our SED fitting results are shifted by less than 0.1 dex on average. The library includes nebular emission, which may contribute significantly to the broadband flux of the dwarf galaxies in our sample. We adopt an exponentially declining star formation history (SFH):

$$\mathrm{SFR}(t) \propto e^{-(t-t_0)/\tau}. \quad (2)$$

We choose this relatively rigid SFH (two free parameters, the onset of star formation t_0 and the timescale of decay τ) in order to achieve reasonable computation times when the number of regions to be fit is high. Such a rigid choice of the SFH functional form has the potential to bias SFH recovery, and so we note that the main goal of our analysis is to diagnose the relative change in star formation surface density and star formation efficiency between normal, high surface brightness dwarfs and UDGs, not to provide comprehensive stellar population synthesis properties for UDGs. We will return to this point more comprehensively in Section 4 when we consider validation tests for this method.

The composite stellar population (CSP) model library spans ages between 2 Myr and 12 Gyr and timescales (τ) between 0.3 and 10 Gyr. Each axis consists of 50 logarithmically spaced values. We precompute both the UV-optical spectra and the fluxes through the GALEX and HSC bands for each model in the library. During fitting, we linearly interpolate between precomputed library fluxes to obtain the predicted GALEX and HSC fluxes for arbitrary choices of t_0 and τ. Because we use

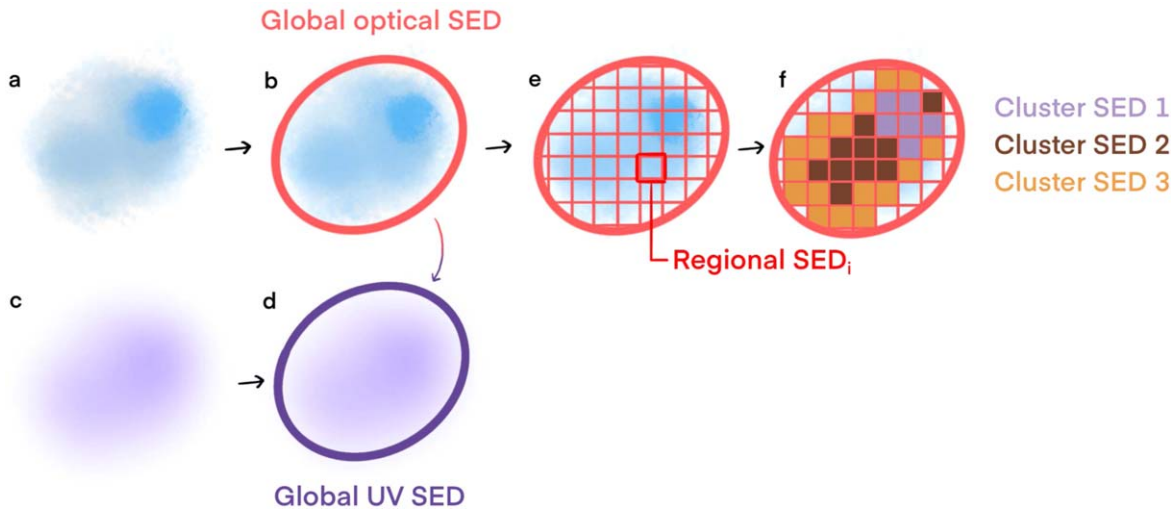

Figure 5. A schematic layout of the fitting technique used in this work. At left, we represent the high-resolution optical data and low-resolution UV data (panels (a) and (c), respectively). Panels (b) and (d) represent the global fit between the optical and UV data; in this step, the apertures are matched between the optical and UV data. Panel (e) shows the spatial division of the optical data into regions in which regional SEDs are measured. Panel (f) shows the clustering of these spatial regions into three representative clusters; these cluster SEDs will be fit jointly with the global UV photometry (panel (d)).

precomputed library fluxes at a fixed distance of 10 Mpc, this induces a small k-correction error in the galaxy sample. However, the most distant galaxies in our sample are at 120 Mpc, and so the k-correction error induced is negligible.

3.2. Defining Global, Regional, and Cluster SEDs

The first step in executing a joint fit between the optical and UV photometry is to establish the apertures in which we measure the optical and UV photometry. To obtain consistent optical photometry, we PSF match the HSC imaging with the worst seeing. To do so, we use the Fourier transform-based implementation of photutils with a cosine bell window function ($\alpha = 3$) to compute matching kernels between the other optical bands and the band to which we will match the PSF. We model the PSFs measured by the HSC pipeline (which produces PSF postage stamps with spatial extents of about $7''$) as two-dimensional Moffat functions. We choose to simplify the PSF model to Moffat functions in order to prevent the emergence of imaging artifacts during the matching process caused by high-frequency features in the original pipeline-produced PSFs. We additionally correct for galactic extinction in all UV and optical photometry presented in this work using the measurements of Schlafly & Finkbeiner (2011) via the associated online service (IRSA 2022).[5]

We then define the global aperture of the galaxy using sep, a python implementation of the segmentation algorithm used in SExtractor (Bertin & Arnouts 1996). In all cases, we use the HSC-g band as the detection band, with a detection threshold of 5σ over the variance image supplied by the HSC pipeline. We define the elliptical global aperture as

$$c_{xx}(x-\bar{x})^2 + c_{yy}(y-\bar{y})^2 + c_{xy}(x-\bar{x})(y-\bar{y}) = 3^2, \quad (3)$$

where $\bar{x}$ and $\bar{y}$ are the light-weighted central coordinates of the galaxy and c_{xx}, c_{yy}, and c_{xy} are the standard SExtractor ellipse parameters

$$\begin{aligned} c_{xx} &= \frac{\cos^2\theta}{a^2} + \frac{\sin^2\theta}{b^2} \\ c_{yy} &= \frac{\sin^2\theta}{a^2} + \frac{\cos^2\theta}{b^2} \\ c_{xy} &= 2\cos\theta\sin\theta\left(\frac{1}{a^2} - \frac{1}{b^2}\right), \end{aligned} \quad (4)$$

where a and b are the semimajor and semiminor axes, respectively, and θ is the position angle of the galaxy measured counterclockwise from the horizontal (in image coordinates). This global aperture step is shown visually in step b in Figure 5—the global aperture defined in step b using the optical data is then applied to the UV imaging to derive the global UV SED (step d). We choose not to PSF match the optical data to the UV data to maintain the spatial resolution of the optical data in order to hold the input images consistent between the global and spatially resolved SED fitting. If we did perform PSF matching to the GALEX imaging to compute the global optical photometry, we have verified that the changes would be negligible, with a mean fractional deviation in flux of 0.03 and a standard deviation of −0.02.

Next, to define the regional boundaries for the optical photometry, we lay a grid of fixed size over the cutout image, as shown in step e in Figure 5. The box length of this grid is set to be no less than twice the FWHM of the PSF-matched images, and is increased iteratively until the median signal-to-noise ratio (S/N) of the SEDs measured in the regions is at least 3. To remove regions where a reliable SED cannot be measured at the required spatial scales, we remove the bottom 5% faintest regions. We also mask regions with $(g-i) > 0.8$ and generate additional masks for UDGs, whose diffuse structure and large on-sky sizes make standard deblending routines unreliable. We verify that this pruning does not affect the total inferred mass and SFR in Section 4.

Because the size of the regions is small compared to the size of the galaxy, it is unsurprising to note that many of the regional SEDs are identical to each other to within their

[5] Galactic extinction measurements were accessed via https://irsa.ipac.caltech.edu/applications/DUST/.

photometric errors. To decrease the number of parameters to fit, and to increase the S/N of the SEDs that we fit, we group the regions (step e) into clusters of similar SEDs (step f). We group the regions into clusters using k-means clustering, initially with three clusters. If any cluster has an S/N < 10, we combine the low-S/N cluster with the closest high-S/N cluster (here defining closeness by the ℓ^2 norm[6] over the optical SEDs). Next, we must verify that the cluster SEDs adequately represent their input regional SEDs. We use the metric $z^j_{b,i} = |f_{b,i} - \bar{f}^j_b| \Big/ \sqrt{\sigma^2_{f_{b,i}} + \sigma^2_{\bar{f}^j_b}}$, where $f_{b,i}$ is the flux in band b measured in region i, while $\bar{f}^j_b$ is the flux in band b measured in cluster j. $\sigma^2_{f_{b,i}}$ and $\sigma^2_{\bar{f}^j_b}$ refer to the uncertainty on the respective flux measurement. We impose the condition $z_{b,i} < 2$ for all bands $b \in \{g,r,i,z,y\}$ and all regions i assigned to cluster j for each cluster in the galaxy. If the clustering result fails this verification, we rerun the clustering process with an additional cluster at the k-means step. We allow up to five clusters, at which point the clustering assignment is accepted regardless of verification status. In practice, only one galaxy (the UDG AGC 223246) is fit with the maximum five clusters.

3.3. SED Fitting

With our PSF-matched photometry and apertures in hand, we are now ready to begin the SED fitting. For all of our fitting, we use the Markov Chain Monte Carlo implementation of emcee (Foreman-Mackey et al. 2013). We adopt a flat prior over positive values for the amplitude of each cluster SED, a flat prior between 0 and 13.6 Gyr for τ (see Equation (2)), and a log-normal prior over A_V distributed as $\log_{10}(A_V) \sim \mathcal{N}(0, 0.1)$. In our joint fitting step, where multiple amplitudes and τ values are being inferred, the prior is the same for each individual parameter.

We first perform a global SED fit using both the optical and UV photometry to constrain the reddening, A_V, and to provide an estimate of the total stellar mass and SFR. We adopt a Gaussian likelihood, defined as

$$\log \mathcal{L} \propto -\frac{1}{2}\sum_b^M \frac{(f_b - \hat{f}_b)^2}{\sigma^2_{f_b}} + \log(\sigma^2_{f_b}), \quad (5)$$

where f_b refers to the flux of the bth band out of M bands ($M = 7$ for our fiducial case), $\hat{f}_b$ is the predicted model flux, and σ_{f_b} is the uncertainty in the bth band. We measure σ_{f_b} directly from the variance images of HSC-SSP added in quadrature to an extra uncertainty of $0.05 f_b$. In this step we run emcee for 1500 iterations with 32 walkers, discarding the first 400 steps. The only parameter from this fit that survives as a final result is the reddening, which is used to the joint fit as a fixed parameter. We find no difference in the A_V estimated for the UDGs and the NSA galaxies at $M_\star < 10^9 M_\odot$: the 50th (16th and 84th) percentile of the A_V distribution is $A_V = 0.17$ (0.04, 0.37) for the UDGs and $A_V = 0.18$ (0.05, 0.38) for the NSA dwarfs at $M_\star < 10^9 M_\odot$. Unsurprisingly, the NSA galaxies at higher stellar mass have systematically higher estimated reddening—$A_V = 0.67$ (0.55, 0.99).

Next, we compute the flux in the N SED clusters defined as above. At this stage, the model consists of a set of N models across M bands. The likelihood is computed as follows:

$$\log \mathcal{L} \propto -\frac{1}{2}\sum_{i\in UV} \frac{\left(\sum_j^N f_{i,j} - \sum_j^N \hat{f}_{i,j}\right)^2}{\sum_j^N \sigma^2_{f_{i,j}}} + \log\left(\sum_j^N \sigma^2_{f_{i,j}}\right) + -\frac{1}{2}\sum_j^N \sum_{i\in Opt} \frac{(f_{i,j} - \hat{f}_{i,j})^2}{\sigma^2_{f_{i,j}}} + \log(\sigma^2_{f_{i,j}}), \quad (6)$$

where i refers to the bandpass index and j refers to the cluster index. In other words, we retain a Gaussian likelihood wherein the UV bands (FUV and NUV) are compared against the sum of the regional models, whereas the optical bands (*Opt* in Equation (6); g,r,i,z,y) are compared against the appropriate regional models. In this step, the walkers are initialized with the positions drawn from the posterior of the global SED fit; the amplitude of each cluster SED is additionally multiplied by the mean ratio between the flux in the cluster SED and the global SED over the optical bands. In this step, we run emcee for 20,000 iterations with at least 32 or $2N + 1$ walkers, discarding the first 5000 steps.

From this process we estimate the total stellar mass and SFR for each cluster SED. We then convert these to stellar mass and SFR surface densities assigned to each regional SED by multiplying by the ratio of the flux in the regional SED and the flux in its corresponding cluster SED, and dividing by the physical area subtended by the region.

We show an example of the fitting procedure for the galaxy NSA 5449 in Figure 6. We also show an abbreviated gallery of fitting results in Appendix A for a set of galaxies that span the morphologies seen in the NSA and UDG samples.

4. Method Validation

In order to apply the framework constructed in the previous section to our galaxy samples, we must first take the necessary step of validating that our method is able to accurately deliver the quantities of interest to this study—namely, maps of the star formation and stellar mass surface densities down to the spatial resolution of HSC.

An equally important step is to lay out the quantities that we are *not* attempting to constrain with this modeling. The age, stellar metallicity, and detailed (flexible) SFH of the galaxies are all parameters that may be estimated from SED fitting. However, it has been shown that the exponentially declining tau model is an imperfect model of SFHs at large, both due to its overall rigidity and that it, by definition, ties early and late star formation (Simha et al. 2014; Carnall et al. 2019). Thus, we stress that our main goals, and the subjects of our verification tests, will be the estimation of the SFR and stellar mass surface densities, and not a detailed interrogation of the SFH and enrichment of the galaxies in our sample.

4.1. Intra-sample Comparisons

We first consider an internal comparison between the SFR and stellar masses measured from the global UV+optical SED fitting (step b and step d in Figure 5) and the integrated SFR and stellar masses obtained by summing the properties inferred from the cluster SED fitting (step f). In Figure 7, we show the integrated estimates of stellar mass (top) and SFR (bottom) for the UDGs (red) and NSA galaxies (purple). In all cases, we find good internal consistency between the initial SED fit on the

[6] Where the ℓ^2 norm is the difference between the SED flux and reference flux $\sqrt{\sum_k^K |f_k - f_{\rm ref}|^2}$ over the K optical bands.

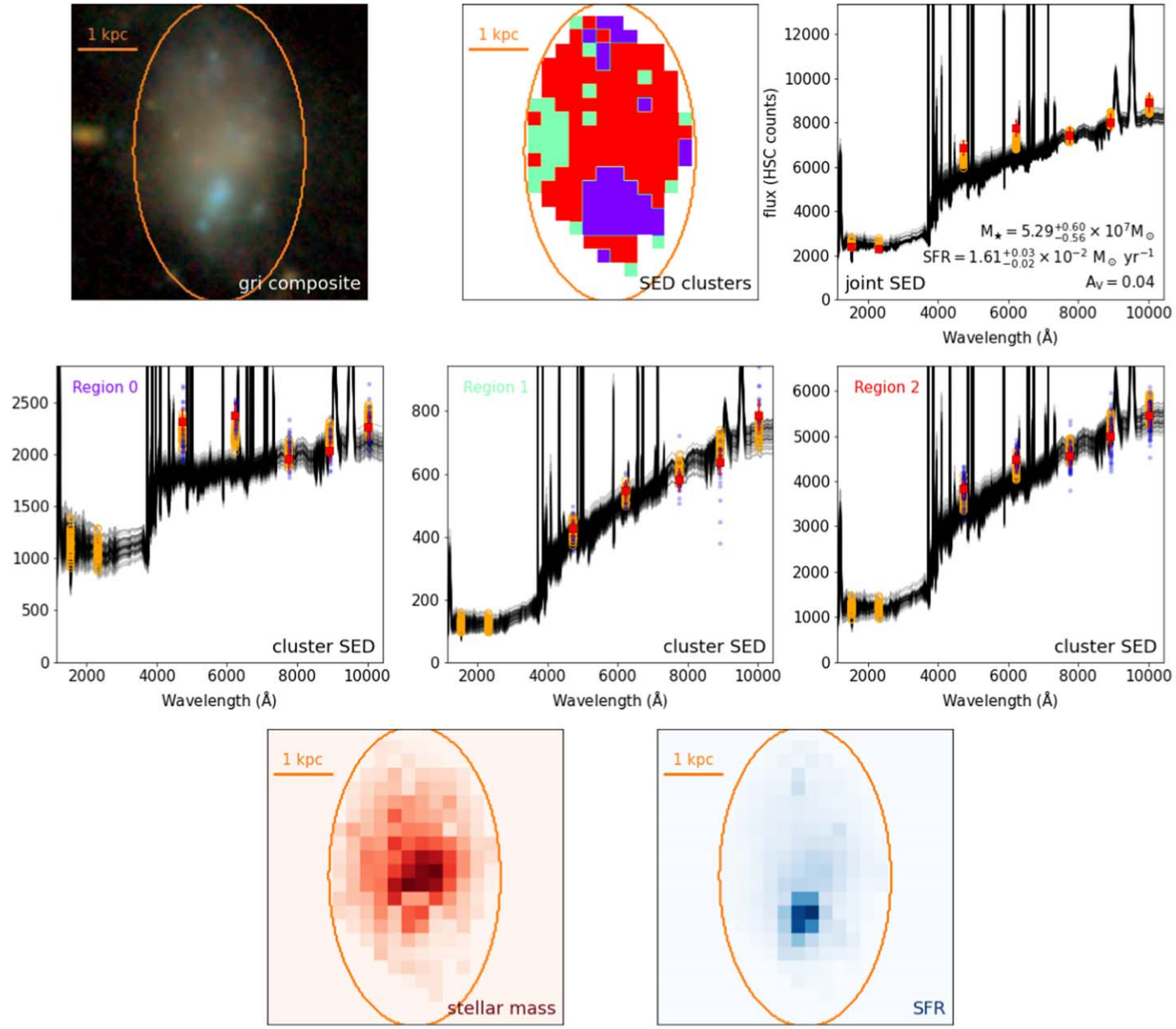

Figure 6. An example of the fitting process for one of the NSA galaxies (NSA ID 5449). Top row: from left, the HSC *gri*-composite image, the SED cluster map (analogous to panel (f) of Figure 5), and the joint UV-optical SED fit. The joint model SED is the result of fitting the spatially resolved (cluster) optical photometry and global UV photometry. The black curves show the model spectra, while the orange points show the model photometry for each filter. The red points show the global UV-optical photometry. The model fitting and figure fluxes are computed as HSC counts. Middle row: optical-only results for the individual cluster SEDs. The color of the title text corresponds to the color of the region in the top middle panel; the format is equivalent to the joint SED fit (top right), with the addition of the SEDs measured in individual spatial regions (i.e., regional SEDs) as blue points. Here, the red points show the cluster SEDs (i.e., the sum of the regional SEDs) rather than the global photometry. Bottom row: the resultant stellar mass (left) and SFR (right) maps.

global photometry and the final model SED of the spatially resolved method.

We additionally compare the stellar mass and SFR estimates obtained from our spatially resolved SED fitting method to the catalog NSA stellar masses and FUV-only SFRs in Figure 8. The FUV-only SFRs are computed from the catalog GALEX measurements using the prescription of Kennicutt (1998), i.e.,

$$\mathrm{SFR}(L_{\mathrm{FUV}}) = 1.4 \times 10^{-28} \frac{L_{\mathrm{FUV}}}{\mathrm{erg\ s^{-1}\ Hz}}. \quad (7)$$

Both the catalog stellar mass estimates and the FUV-only SFRs are also in good agreement with the results of our spatially resolved fit.

Although we lack truly spatially resolved spectroscopic measurements for the galaxies in our sample, we do have access to one quasi-resolved measurement for the NSA sample—the SDSS 3″ fiber spectra. Because our galaxies exceed the SDSS fiber size, the SDSS spectroscopic measurements do contain information about the spatial distribution of star formation within the galaxy, albeit in a very limited capacity. In the right panel of Figure 8 we show a comparison between SFRs derived from the SDSS fiber spectroscopy of the NSA galaxies and SFRs we compute by integrating our SFR maps over SDSS-like apertures. The SDSS spectroscopy we reference are 3″ diameter fiber spectra; we use the NSA catalog line fluxes in this

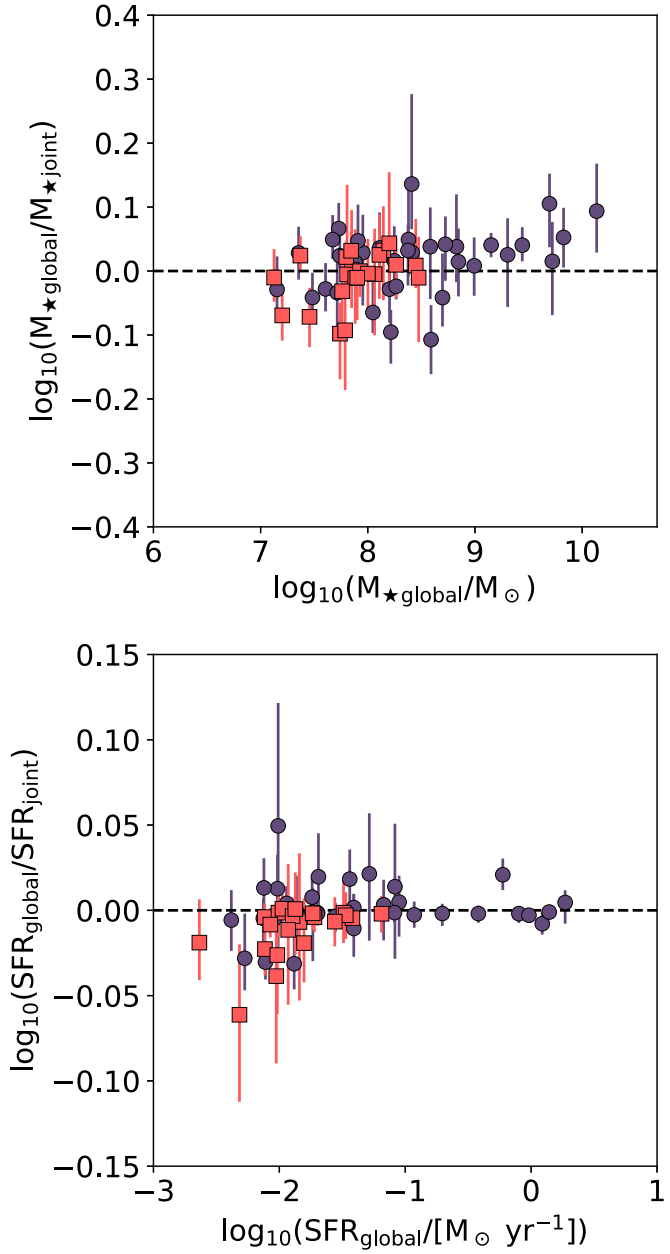

Figure 7. Top: a comparison between the best-fit stellar masses of the NSA (purple) and UDG (red) samples using the difference between results derived from the spatially resolved and global photometry (y-axis) and the global optical photometry (x-axis). Bottom: the same as above, but for SFR.

comparison. In particular, we use the catalog Hα flux to compute Hα-derived SFRs within the SDSS aperture following Calzetti (2013) with a Kroupa (2001) IMF:

$$\mathrm{SFR}(L_{\mathrm{H}\alpha}) = 5.5 \times 10^{-42} \frac{L_{\mathrm{H}\alpha}}{\mathrm{erg\ s^{-1}}}. \quad (8)$$

Although the 100 Myr averaged SFRs we produce via our SED fitting are not completely analogous to the Hα SFRs derived from the SDSS spectra (which probe timescales closer to $\lesssim$10 Myr), we expect that the two should be well-correlated. Indeed, we find that the SFRs we compute from the central three arcseconds of our SFR maps are in good agreement with the SDSS spectroscopic measurements, with a scatter on the same order as the physical variation between UV and Hα SFRs measured from Local Volume dwarfs (Karachentsev et al. 2021, red line in the right panel).

4.2. Inter-sample Comparisons to the Literature

We also find good agreement between our results and literature measures of the integrated stellar mass, SFR, and A_V for the two low surface brightness galaxies presented in Greco et al. (2018a), though we do not include these galaxies in this work because they lack H I measurements.

Finally, we compare to spatially resolved measurements of stellar mass, SFR, and H I in nearby samples of dwarfs from the literature. In Figure 9, we show a comparison between radial profiles of stellar mass surface density (left) and SFR surface density (right) as derived from our SED fitting method as compared to the directly measured results of Leroy et al. (2008). Our results are shown as solid curves, and the Leroy et al. (2008) profiles are shown as dashed curves; all curves are colored by total stellar mass. Encouragingly, we find good agreement in both the shape and normalization between our inferred radial profiles and the directly measured results of Leroy et al. (2008), indicating that our method is able to recover not just the total amount of stellar mass and SFR, but the distribution of these quantities.

5. Results

With our methodology in hand, we may now return our focus to the physical question at hand. In Section 2.1, we demonstrated that although UDGs have low globally averaged stellar mass and SFR surface densities, their H I surface densities are comparable to those of NSA galaxies. Now, we can consider the cause of the low SFE(H I) of UDGs —and in particular whether this inefficiency persists to sub-kiloparsec scales—as well as the relationship between UDG structure and H I content. For the interested reader, we include a table of selected SED fitting results for the sample in Table 1.

5.1. Efficiency and Distribution of Star Formation in UDGs

In the top row f in Figure 10, we show the relation between the estimated $\Sigma_{\mathrm{H\,I}}$ and Σ_{SFR} at 500 pc, 1 kpc, and global scales from left to right (we note that, for reasons of visual continuity, the bottom right panel of Figure 10 is identical in content to the bottom panel of Figure 3). We compute 1 kpc and 500 pc average stellar mass surface density and SFR surface density maps by placing a grid of length 1 kpc or 500 pc (at the distance of the galaxy) over the stellar mass and SFR maps produced via SED fitting. We do not compute average quantities over length scales less than the regional SED box size for each galaxy. For the 1 kpc and 500 pc regions, the H I surface density is estimated using the central position of the region and the Sérsic profile estimated for the galaxy as described in Section 2.3. From this figure, the reader may immediately notice that the shift in Σ_{SFR} persists down to 500 pc; there are no regions in the area-weighted census of the UDG distribution of SFR surface density that match the vigorously star-forming SFR surface densities observed in NSA dwarfs.

The persistence of the discrepancy of star formation activity outcomes as a function of H I surface density indicates that it is not simply a matter of the distribution of star formation that drives the apparently low star formation

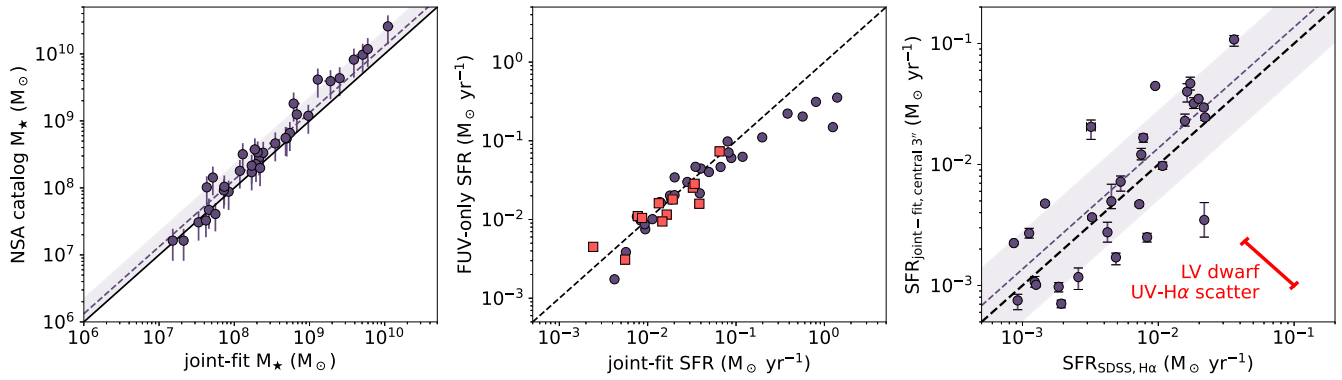

Figure 8. Left: a comparison between the stellar masses of the galaxies in this work (x-axis) and their catalog NSA stellar masses. The dashed line and shaded regions show the median, and range between the 16th and 84th percentiles of the deviation $\log_{10}(M_\star/M_\odot) - \log_{10}(M_{\star,NSA}/M_\odot)$. Middle: the same, but for SED fitting-derived SFRs and FUV-only SFRs as computed from the catalog GALEX measurements using the SFR(FUV) prescription of Kennicutt (1998). Right: a comparison between SFRs derived from the Hα fluxes measured from SDSS 3" fiber fibers (x-axis) and the total SFR within the central 3" of our SED fits (y-axis, red). The dashed black line denotes a 1:1 relation. As in the left panel, the dashed purple line and shaded purple regions show the median, and range between the 16th and 84th percentiles. SFRs derived from Hα measure star formation over a shorter timescale ($\sim$10 Myr) than our SED fits (100 Myr), and some physical scatter is expected as a result; we show the standard deviation (in logarithmic space) of the difference between Hα-derived and FUV-derived SFRs for a set of Local Volume dwarfs from Karachentsev et al. (2021) as a visual aid to the reader in gauging the scatter.

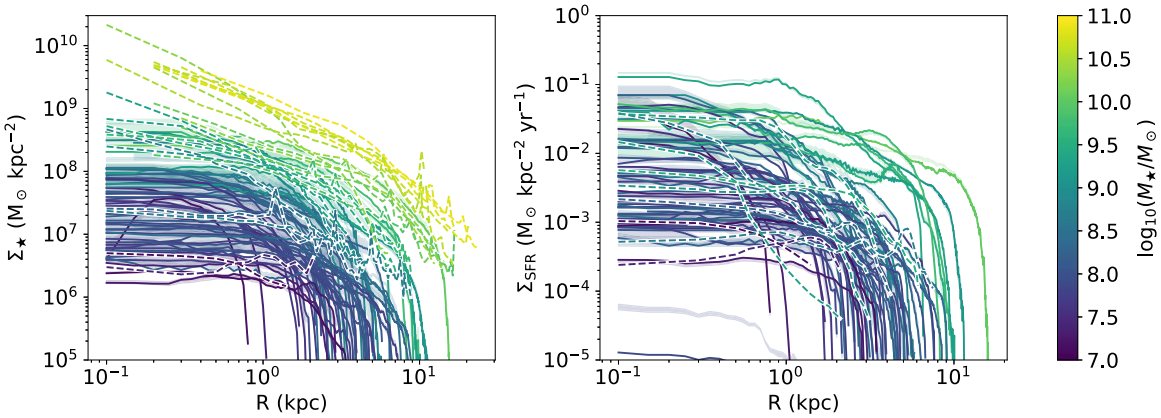

Figure 9. A comparison between radial profiles in stellar mass surface density (left) and SFR surface density (right) from our SED fitting method (solid curves) as compared to direct measurements from Leroy et al. (2008, dashed curves). The color of the curves shows the integrated stellar mass of the galaxy in all cases. We find that there is good agreement between our radial profiles and the directly measured profiles in both amplitude and extent.

Table 1
Selected SED Fitting Results

ID	R.A. (deg)	Decl. (deg)	Dist (Mpc)	$M_{\rm H\,I}$ ($10^8\,M_\star$)	$M_\star$ ($10^8\,M_\star$)	SFR ($10^{-3}\,M_\star yr^{-1}$)	A_V (mag)	$R_{1/2,\star}$ (kpc)	$R_{1/2,g}$ (kpc)
NSA 16938	140.433	4.374	85.81	13 ± 2.8	$5^{+0.66}_{-0.58}$	$40^{+1.9}_{-1.5}$	$0.15^{+0.12}_{-0.099}$	1.9 ± 0.38	1.8 ± 0.32
NSA 11919	132.078	1.263	27.67	1.3 ± 0.42	$1.3^{+0.19}_{-0.092}$	$5.7^{+0.35}_{-0.24}$	$0.15^{+0.17}_{-0.1}$	1.7 ± 0.19	1.9 ± 0.1
NSA 16993	143.969	4.017	81.05	36 ± 4.2	$51^{+7.8}_{-9}$	$800^{+8.5}_{-10}$	$0.64^{+0.059}_{-0.051}$	2.7 ± 0.48	3.5 ± 0.3
NSA 13797	174.755	1.336	24.92	1.9 ± 0.58	$0.43^{+0.042}_{-0.034}$	$35^{+1.4}_{-1.1}$	$0.079^{+0.036}_{-0.035}$	0.71 ± 0.12	0.6 ± 0.093
AGC 334353	345.863	1.704	71.40	12 ± 1.9	$1.2^{+0.19}_{-0.18}$	$12^{+1.1}_{-1.2}$	$0.1^{+0.11}_{-0.071}$	2.1 ± 0.28	2.5 ± 0.27
AGC 334349	345.277	1.998	51.10	5.2 ± 0.83	$0.82^{+0.12}_{-0.11}$	$10^{+0.76}_{-0.78}$	$0.087^{+0.097}_{-0.064}$	1.4 ± 0.2	1.9 ± 0.19
AGC 103435	3.838	1.075	28.50	1.9 ± 0.4	$0.14^{+0.015}_{-0.012}$	$8.6^{+0.19}_{-0.15}$	$0.18^{+0.059}_{-0.058}$	1.5 ± 0.11	1.8 ± 0.11
AGC 198540	141.308	3.313	63.30	13 ± 1.8	$1.4^{+0.42}_{-0.23}$	$13^{+0.68}_{-0.8}$	$0.14^{+0.11}_{-0.092}$	1.9 ± 0.26	2 ± 0.24

Note. Table 1 is published alongside this article in its entirety in the machine-readable format. A portion is shown here for guidance regarding its form and content. (This table is available in its entirety in machine-readable form.)

efficiency (as a function of atomic gas) in the UDG sample. Rather, it appears to be a generic property of star formation in our sample of UDGs. The question, then, of whether a more comprehensive understanding of star formation can explain this low star formation efficiency will naturally arise to the reader. This question is the central topic of Paper II, in which we will examine the impact of the UDGs' peculiar stellar structure on their star formation activity within the framework of pressure-regulated, feedback-modulated star formation (Ostriker et al. 2010; Kim et al. 2011; Ostriker & Shetty 2011; Kim et al. 2013; Kim & Ostriker 2015; Kim et al. 2017).

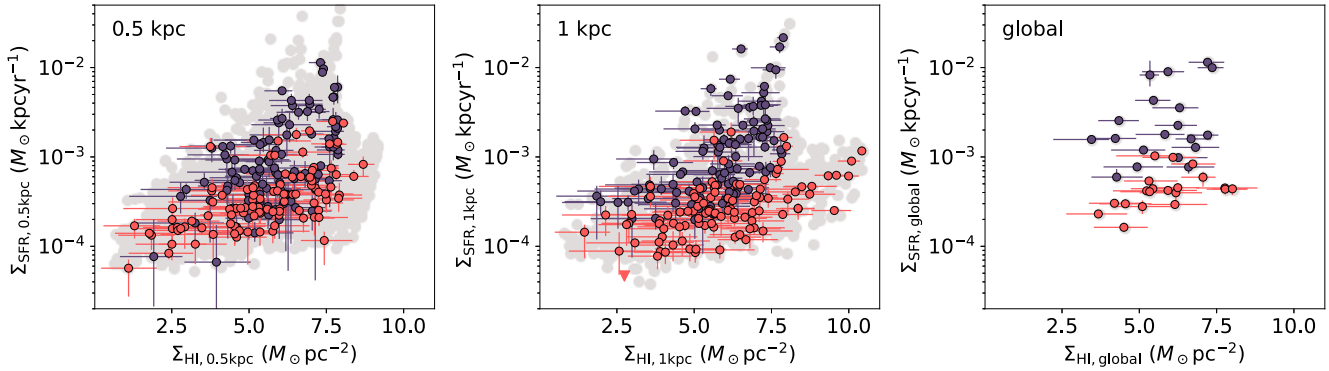

Figure 10. A comparison between H I surface density estimates and SFR surface density measurements averaged over 500 pc, 1 kpc, and global scales. In all panels, we only show NSA galaxies that are within the stellar mass range of the UDG sample (i.e., $M_\star < 3 \times 10^8\,M_\odot$). For visual clarify, we show a random subset of (at most) 70 points for each sample with individual error bars and colored by sample source; we show the full sample as the underlying gray scatter. Here, we demonstrate that the low SFE(H I) that characterizes the globally averaged properties of UDGs persists down to sub-kiloparsec scales.

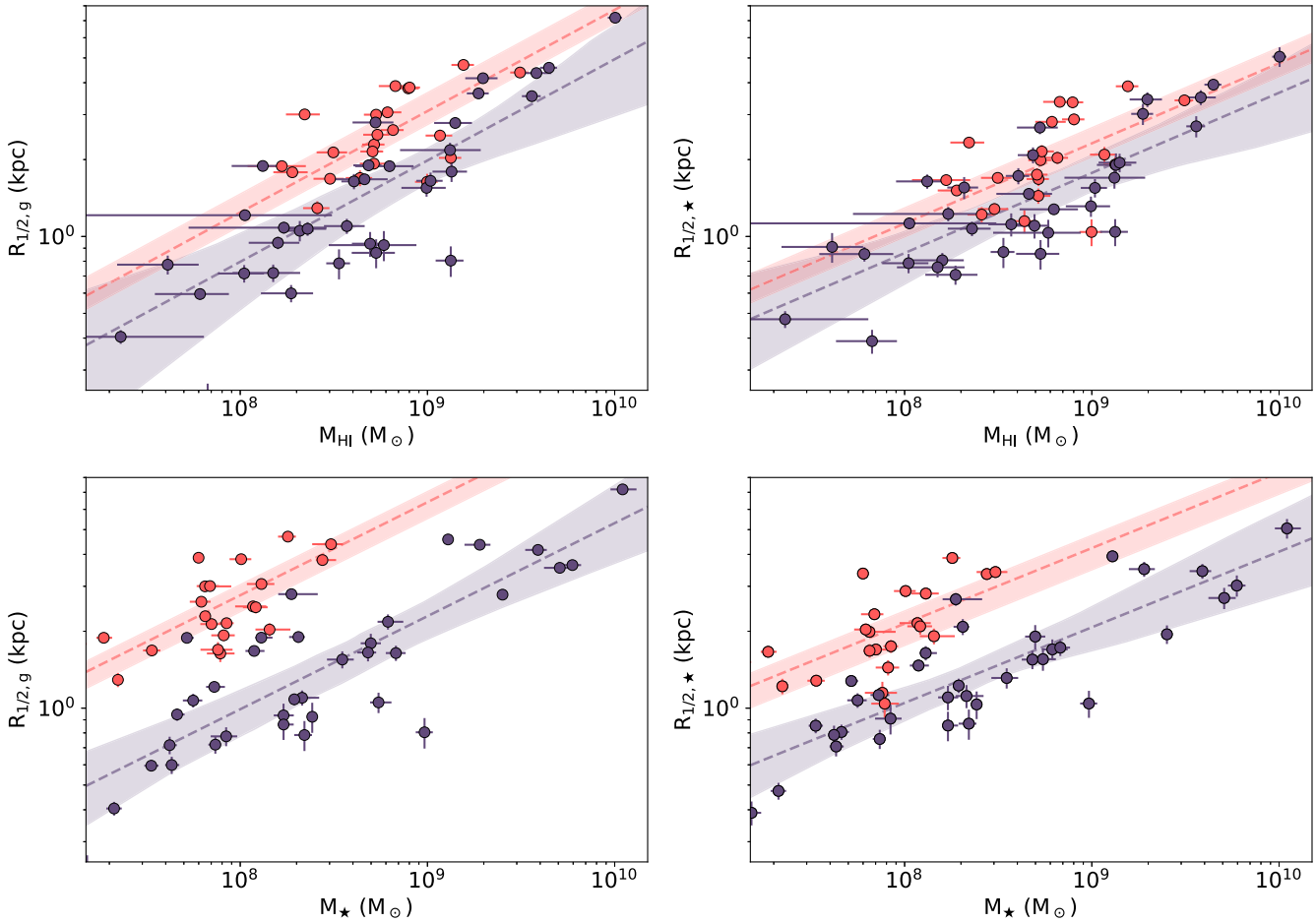

Figure 11. A comparison between various measures of galaxy mass and galaxy size; the top row shows size as a function of H I mass, while the bottom row shows size as a function of stellar mass. The left column shows size as measured by the HSC-*g* band half-light radius, while the right column shows size as measured by the half-stellar mass radius. In each panel, the purple dashed line shows the least squares power-law fit to the NSA galaxies. The red dashed line shows the least squares fit to the UDG sample when the index of the power law is held fixed to that of the NSA dwarf fit. The shaded regions span the 16th–84th percentiles as estimated from bootstrap resampling. As one expects, the UDG sample is large in size for their stellar masses. However, their half-stellar mass radii are unremarkable for their H I masses.

We note that the minimum region size over which we can measure Σ_{SFR} and $\Sigma_\star$ is set by the distance of the galaxy and the angular scale over which we measure our regional SEDs (panel e, Figure 5). In particular, the galaxies for which we are able to measure 500 pc averages tend to be the closest galaxies in our samples, and are thus skewed toward lower stellar masses. However, we find that this effect does not impact the results presented here, as the majority of galaxies affected are more massive than the UDGs in this sample. In particular, there are five galaxies within the stellar mass range of the UDGs that

are affected. Four are themselves UDGs (AGC 227965, AGC 322019, AGC 198543, and AGC 238961), and one is an NSA dwarf (NSA ID 17750).

5.2. H I Properties of the UDG Sample

In addition to their star formation efficiency, it is of interest to understand the relationship between the stellar structure of these H I-rich UDGs and their integrated gas properties. In Figure 11, we show the H I mass–size relation of the UDG and NSA samples for two definitions of *mass* and *size* (i.e., four total combinations). The left column shows sizes measured as g-band half-light radii, while the right column shows sizes measured as half-mass radii, where we refer to the radius that contains half the *stellar* mass of the galaxy as the half-mass–radius. The half-light, half-mass, and half-SFR radii reported in this work are measured over the same area of the galaxy as our derived stellar mass and SFR maps (i.e., only in pixels where the stellar mass surface density is nonzero). We use the PSF-matched HSC images with the same machinery as the half-mass and half-SFR radius measurements. The half-light radii reported in this work are thus not completely analogous to effective radii measured using other methods (e.g., Sérsic fitting). In particular, though there is no systematic offset between the two methods ($\bar{\Delta R}/R = -0.05$ for the full sample, and -0.06 (-0.04) for the NSA (UDG) subset), there is significant scatter ($\Sigma_{\Delta R/R} = 0.15$ for the full sample, and 0.13 (0.19) for the NSA (UDG) subset). We estimate the uncertainty in our half-mass and half-light radius measurements by adding in quadrature the physical size of the PSF FWHM and the standard deviation of the radii due to the uncertainty in the stellar mass fits/photometry, respectively. The top row shows H I mass, while the bottom shows stellar mass. In essence, one can think of the bottom left panel as the *canonical* mass–size relation (stellar mass versus light-weighted size).

When one considers the size of UDGs as a function of their integrated stellar mass, it is immediately apparent that they are systematically larger than the NSA sample in both their light-weighted and mass-weighted sizes. This is unsurprising, of course, given that UDGs are selected for their low surface brightnesses and large physical sizes. When one considers UDGs as a function of their integrated H I mass, however, the picture changes. In particular, we see no significant difference in the relation between the H I masses and half-mass (stellar) radii of the UDG and NSA samples. There is, however, some evidence that the half-light radii of UDGs remain elevated with respect to the NSA sample at fixed H I mass.

5.3. Color–mass Relation of UDGs

Though not the main focus of this work, we are able to directly compare the color–mass relation of gas-rich UDGs and normal dwarfs as a byproduct of the SPS fitting presented above. Standard color–mass relations (e.g., Bell et al. 2003; Into & Portinari 2013) have been assumed in the literature for color-based estimates of UDG stellar mass (e.g., Mancera Piña et al. 2019a; Karunakaran et al. 2020; Marleau et al. 2021), but it has not been directly shown that these optical color relations are applicable to the UDG population. In particular, the canonical color–mass relations are typically calibrated for and tested on largely massive galaxies; it is thus of practical importance for both the UDG community and general dwarf galaxy community to test the applicability of these relations on the extreme pockets of the dwarf population (e.g., UDGs, blue compact dwarfs, etc.).

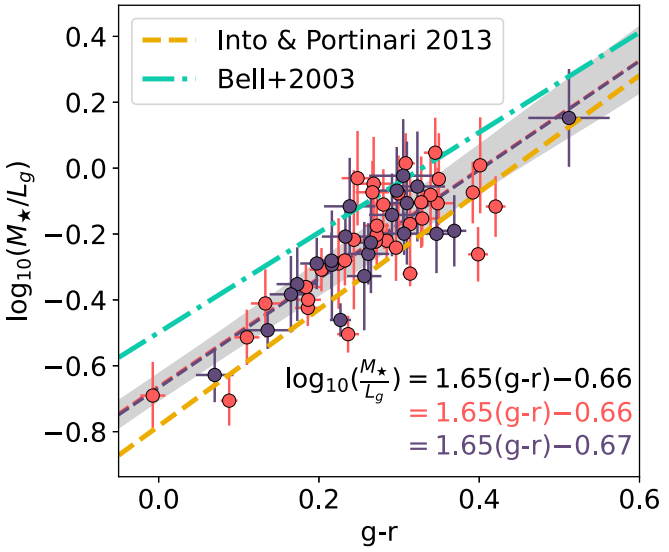

Figure 12. Optical color vs. stellar mass-to-light ratios in the HSC-g band computed for our UDG (red) and NSA (purple) samples. We find no significant difference in the color–mass relation between the two samples, and additionally find the samples to be reasonably well described by color–mass relations from the literature (Into & Portinari 2013 as the dashed line, Bell et al. 2003 as the dotted line).

In Figure 12, we show the global (i.e., light-weighted) g-band mass-to-light relations of the dwarfs in this work (as usual, red points indicate the UDG sample while purple points indicate the spectroscopic dwarf sample). We calculate stellar mass-to-light ratios by computing the $g_{\rm HSC}$ luminosity and stellar mass from the global optical SED of each galaxy (panel b in Figure 5). The $g_{\rm HSC} - r_{\rm HSC}$ colors are measured using the same SED used to derive the stellar mass-to-light ratio.

We find that there is no offset between the H I-selected UDG sample and the NSA dwarf sample, and that the samples are well described by a relation that lies between the Into & Portinari (2013) and Bell et al. (2003) color–mass relations. For completeness, we list our ordinary least squares parameters and standard errors here, where we define $\eta \equiv (M_\star/L_g)(L_\odot/M_\odot)$. We avoid the standard choice of Υ as it is reserved for a parameter linking star formation and midplane pressure in Paper II.

$$\begin{aligned}
\log_{10}\eta_{\rm all} &= 1.59 \pm 0.14(g-r) - 0.65 \pm 0.04 \\
\log_{10}\eta_{\rm UDG} &= 1.65 \pm 0.21(g-r) - 0.66 \pm 0.06 \\
\log_{10}\eta_{\rm NSA} &= 1.55 \pm 0.20(g-r) - 0.64 \pm 0.06, \qquad (9)
\end{aligned}$$

the exact calibration of this relation is, of course, dependent on both the photometric bands used and IMF assumptions. We in particular note that Into & Portinari (2013) and Bell et al. (2003) are calibrated for SDSS g and r bands, which are similar but not identical to HSC g and r bands). Regardless, we have demonstrated that UDGs do not lie systematically off of the color–mass relation of NSA dwarfs, and that both samples are in relatively good agreement with previous relations from the literature.

6. Discussion

Taken altogether, we find that our sample of H I-rich UDGs is characterized by low star formation efficiencies (where $\mathrm{SFE(H\,I)} \equiv \Sigma_{\mathrm{SFR}}/\Sigma_{\mathrm{H\,I}}$) down to sub-kiloparsec scales, and that UDGs are generally incapable of supporting the vigorous star formation seen in the normal NSA dwarfs. Intriguingly, although UDGs are large in light-weighted size for their total stellar mass, their stellar mass-weighted sizes are typical for their H I masses. Finally, the stellar mass-to-light ratios of UDGs appear consistent with those of the NSA dwarf sample.

6.1. Implications for UDG Formation

The results presented in this work suggest that H I-rich UDGs are unable to efficiently convert gas to stars or host vigorous star formation. Such low SFR surface densities indicate that UDGs will continue to trail behind the stellar mass build-up of the general dwarf population. This finding, however, does not alone answer the question of *why* certain galaxies fail to trigger vigorous star formation. Several mechanisms have been put forth in the literature to explain the population of field UDGs. For each formation model, we will first discuss the points in which our observations agree with the model predictions before turning toward points of potential conflict.

Feedback-driven expansion. We first consider the picture in which field UDGs are formed via starburst-driven outflows that cause potential fluctuations that in turn lead to net expansion of the stellar population (El-Badry et al. 2016; Di Cintio et al. 2017; Chan et al. 2018). We note that in this section we deal with results from both the Feedback In Realistic Environments (FIRE; Hopkins et al. 2014, and FIRE-2, Hopkins et al. 2018) and Numerical Investigation of a Hundred Astrophysical Objects (NIHAO; Wang et al. 2015) simulations; though both simulations point to feedback-driven expansion as the culprit of UDG formation, the feedback implementation between the two simulations is not identical.

In the NIHAO simulation, such UDGs are expected to retain systematically higher H I fractions with respect to normal dwarfs, in good agreement with our results (Di Cintio et al. 2017). However, two points of potential conflict emerge. First, the radial expansion of the UDG stellar population should enforce a radial age gradient; that is, the older stars should experience more expansion due to having gone through a larger number of inflow/outflow cycles. This picture suggests a relatively centrally concentrated distribution of star formation in UDGs, where the stars experience net expansion while the gas goes through cyclical phases of inflow and outflow. Such behavior is in qualitative conflict with the observation that UDG star formation is both consistently lower than and more radially extended than star formation in NSA dwarfs (see lower panels of Figure 9). However, to our knowledge a detailed study of the star formation extendedness and efficiency has not been done for UDGs created by feedback-driven expansion. Further analysis is necessary to confirm that feedback-driven expansion cannot reproduce this effect (via, e.g., the substantial expansion of stars within 100 Myr of formation).

However, another point of conflict exists between our observations and the feedback-driven expansion picture. Namely, in both FIRE and NIHAO the marked expansion of UDGs is driven by particularly prolonged and bursty star formation histories (Di Cintio et al. 2017; Chan et al. 2018). In this work, we have shown that the lack of vigorous star formation in UDGs is linked to their low stellar mass surface densities; that is, their low SFR surface densities are explainable by their stellar and gaseous structure. Conversely, then, the structure of UDGs makes it difficult to envision a scenario in which they are able to power frequent and vigorous bursts of star formation at late times. This does not, of course, rule out UDG formation via star formation feedback if the star formation behavior of UDGs was markedly different at high redshift than it is in nearby UDGs. Indeed, such a transition has been predicted in models such as that in Trujillo-Gomez et al. (2022). However, these new observations provide new constraints on models which predict star formation feedback to remain vigorous down to $z = 0$.

Early mergers. Another proposed mechanism for field UDG formation is the result of an early merger (more than 8 Gyr ago) that caused an increase in total spin as well as a decrease in central SFR and a redistribution of star formation to large radii (Wright et al. 2021). Like our observed galaxies, the galaxies in the ROMULUS25 simulation are H I-rich for their stellar mass and lie on the integrated SFMS. However, we do not find the lower central specific star formation that Wright et al. (2021) cite as a significant observable manifestation of this formation channel; indeed, the distribution of the specific SFR of the UDGs in our sample is not statistically different than that of the NSA sample at any radius.

High spin halos. Finally, we consider the proposal that UDGs are formed out of the high spin tail of the halo distribution (see, e.g., Dalcanton et al. 1997; Amorisco & Loeb 2016; Rong et al. 2017; Di Cintio et al. 2019; Liao et al. 2019). This formation scenario predicts that UDGs will host ordered H I disks, in line with resolved measurements from the literature (Mancera Piña et al. 2019b, 2020; Gault et al. 2021). There is some suggestion that in this formation scenario, UDGs at $z = 0$ should have generally lower central volumetric gas densities and more radially extended profiles than high surface brightness galaxies at fixed stellar mass (Liao et al. 2019). This may be at odds with observational findings, given that the UDGs in our sample have H I surface densities similar to those of NSA dwarfs (see, e.g., Figure 10, which excludes NSA dwarfs with stellar masses larger than the range probed by the UDG sample) and have been previously suggested to lie on the H I mass–size relation (Gault et al. 2021). Together, these findings imply similar volumetric gas densities between UDGs and NSA dwarfs if there is no systematic difference in disk thickness between UDGs and NSA dwarfs. However, the relationship between UDG and normal dwarf H I disk thickness remains observationally uncertain. We thus underscore that we are not seeking to make a comprehensive comparison between the H I structural properties of observed UDGs and their simulated high spin analogs.

The upshot of the discussion at hand, rather, is that neither the early merger scenario nor the high spin halo scenario are in conflict with the most salient point of our analysis—that once set on a path toward low-efficiency star formation, galaxies like our present-day UDGs are likely to continue to fall behind the stellar mass build-up of the general dwarf population.

6.2. Stellar Structure of Dwarfs at Fixed $M_{H\,I}$

In addition to a comparison with established theoretical models, it is informative to consider what fully empirical statement we may make about the relationship between the H I-

rich UDGs and normal NSA dwarfs. In the preceding sections, we have demonstrated that the stellar half-mass radii of UDGs are typical for their H I masses (see Figure 11)—that is, UDGs are not offset from the mass–size plane for a particular casting of mass (H I mass) and size (stellar half-mass radius). This is contrasted, naturally, to the offset in the normal mass–size plane (stellar mass and half-light radii) by which UDGs are definitionally characterized.

A concordance in the relation between H I mass and stellar mass-weighted size would naturally arise if UDGs were forming stars normally with respect to the spatial distribution of gas, but at decreased star-forming efficiency. To illustrate this idea, let us presume that the spatial distribution of H I in UDGs is normal with respect to high surface brightness galaxies, as has been shown for a number of UDGs in our sample by Gault et al. (2021). As hinted to in the introduction, the driving mechanism behind the low star formation efficiency of UDGs will be further explored in Paper II.

In this picture, a galaxy that will become a UDG will form stars over the same spatial distribution as a galaxy that will become a high surface brightness galaxy, but at lower $\Sigma_{\rm SFR}$—thus becoming a galaxy with a lower total stellar mass. The concordance of the UDG and NSA samples in the H I mass–stellar size plane is then a natural consequence of the comparatively lower star formation efficiency of UDGs. Thus, one mechanism by which to generate the normal sizes of UDGs with respect to their H I masses is for present-day UDGs to have assembled most of their stellar mass via the low SFE(H I) star formation that characterizes their behavior at $z = 0$.

7. Conclusions

Due to their large sizes and low stellar mass surface densities, UDGs are both an extreme outcome of galaxy formation and an extreme environment for star formation. H I-selected UDGs are systematically more gas-rich than their normal dwarf analogs (see Figure 2), and there is evidence that some UDGs have assembled the majority of their stars from extremely dense clumps (Danieli et al. 2021). Understanding the way in which star formation proceeds in UDGs is thus of key interest to both the galaxy evolution and star formation communities.

In this work, we have presented a method that allows us to compute SFR and stellar mass surface density maps over galaxies with known distances using spatially resolved optical data and global UV photometry. We use this method to explore the star formation activity in a sample of nearby ($d < 120$ Mpc) H I-detected UDG dwarf galaxies from Janowiecki et al. (2019), along with an NSA reference sample of normal dwarfs with H I measurements from Bradford et al. (2015). The samples in this work allow us to compare and contrast the star formation behavior of UDGs against NSA dwarfs, providing new clues to the evolutionary pathway of these H I-rich UDGs as well as new tests for star formation theory in extreme (low-density) environments, which we will explore in Paper II.

We find that the globally averaged SFR surface densities of UDGs are low compared to their globally averaged H I surface densities (see Figure 3); this offset could be explained either by a truly lower SFE(H I) in UDGs, or by a difference in the relationship between the distribution of the UDGs' stellar mass and SFR. Our results indicate that the SFE(H I) of the UDGs remains lower than that of NSA dwarfs down to 500 pc scales (see Figure 10 and Section 5.1)—UDGs are indeed less efficient at converting atomic gas (to molecular gas) to stars. In the second paper of this series, Kado-Fong et al. (2022), we will consider the role of the galactic structure of UDGs on their star formation. Indeed, we find that the diffuse structure of UDGs can naturally explain their low SFR surface densities and efficiencies. When the structure of UDGs is considered (rather than the gas content alone), we find that their star formation is quantitatively consistent with star formation in both the NSA sample and in more massive galaxies. As such, we direct the interested reader to Paper II of this series of papers.

Returning to the results at immediate hand, we also consider the relationship between the stellar size and H I mass of UDGs, as compared to NSA galaxies (Section 5.2). We find that although UDGs have large stellar sizes (both light-weighted and mass-weighted) for their total stellar mass, their stellar sizes are largely unremarkable as a function of their H I mass. This superficially surprisingly result can be explained naturally when we consider the previous conclusions of this work: UDGs have fairly normal H I structure and properties, and so the spatial distribution of their star formation is set by those normal gas properties. However, because they form stars at a significantly lower SFE(H I), they form fewer stars overall and thus become large for their total stellar mass.

The low efficiency and low SFR surface densities of UDGs indicate that UDGs will continue to lag behind the general dwarf population in their stellar mass build-up, and thus remain diffuse relative to normal dwarfs. However, this does not answer the question of *why* present-day UDGs first entered the evolutionary path to become UDGs at $z = 0$. While this work alone cannot provide a definitive answer to this question, we may consider the implications of our results on contemporary ideas of UDG formation. The spatially extended star formation of UDGs and apparent inability to power vigorous star formation (high SFR surface densities) are in conflict with the idea of UDG formation via the feedback-driven radial expansion of stars for the picture in which feedback-driven expansion continues even when stellar mass surface density is low. Formation mechanisms that set certain halos down the path toward UDG formation at early times (e.g., the high spin halo scenario or early merger scenario) can more naturally explain the low SFE(H I) cycle seen in the sample of UDGs presented in this work.

A natural extension of this work will be to obtain a larger number of spatially resolved H I measurements of the UDGs in this sample, with a particular focus on the most nearby galaxies in the sample (such that we may maximize the physical spatial resolution). Higher resolution UV-optical data will also allow us to directly probe the physical scales relevant to star formation and cluster populations in these galaxies. Further exploration into the star formation and interstellar medium of these UDGs is crucial to further our understanding of UDGs as an extreme environment for star formation, as well as our understanding of how these extreme objects form.

The authors thank E. Ostriker, C.-G. Kim, and L. Lancaster for insightful comments and discussions that greatly improved this manuscript. We also thank the anonymous referee for their review of this work, which improved the quality of the manuscript. The research of E.K.F. was supported by the Porter Ogden Jacobus Fellowship. J.E.G. gratefully acknowledges support from NSF grant AST-2106730.

Based in part on data collected at the Subaru Telescope and retrieved from the HSC data archive system, which is operated by Subaru Telescope and Astronomy Data Center at the National Astronomical Observatory of Japan.

The HSC Collaboration includes the astronomical communities of Japan, Taiwan, and Princeton University. The HSC instrumentation and software were developed by the National Astronomical Observatory of Japan (NAOJ), the Kavli Institute for the Physics and Mathematics of the Universe (Kavli IPMU), the University of Tokyo, the High Energy Accelerator Research Organization (KEK), the Academia Sinica Institute for Astronomy and Astrophysics in Taiwan (ASIAA), and Princeton University. Funding was contributed by the FIRST program from the Japanese Cabinet Office, the Ministry of Education, Culture, Sports, Science and Technology (MEXT), the Japan Society for the Promotion of Science (JSPS), Japan Science and Technology Agency (JST), the Toray Science Foundation, NAOJ, Kavli IPMU, KEK, ASIAA, and Princeton University.

This paper makes use of software developed for the Large Synoptic Survey Telescope. We thank the LSST Project for making their code available as free software at http://dm.lsst.org.

The Pan-STARRS1 Surveys (PS1) have been made possible through contributions from the Institute for Astronomy, the University of Hawaii, the Pan-STARRS Project Office, the Max-Planck Society and its participating institutes, the Max Planck Institute for Astronomy, Heidelberg and the Max Planck Institute for Extraterrestrial Physics, Garching, The Johns Hopkins University, Durham University, the University of Edinburgh, Queens University Belfast, the Harvard-Smithsonian Center for Astrophysics, the Las Cumbres Observatory Global Telescope Network Incorporated, the National Central University of Taiwan, the Space Telescope Science Institute, the National Aeronautics and Space Administration under grant No. NNX08AR22G issued through the Planetary Science Division of the NASA Science Mission Directorate, the National Science Foundation under grant No. AST-1238877, the University of Maryland, and Eotvos Lorand University (ELTE) and the Los Alamos National Laboratory.

Some of the data presented in this paper were obtained from the Mikulski Archive for Space Telescopes (MAST). STScI is operated by the Association of Universities for Research in Astronomy, Incorporated, under NASA contract NAS5-26555. Support for MAST for non-HST data is provided by the NASA Office of Space Science via grant NNX13AC07G and by other grants and contracts.

Based on observations made with the NASA Galaxy Evolution Explorer. GALEX is operated for NASA by the California Institute of Technology under NASA contract NAS5-98034. The specific observations analyzed can be accessed via 10.17909/h19r-ab55.

This research has made use of the NASA/IPAC Infrared Science Archive, which is operated by the Jet Propulsion Laboratory, California Institute of Technology, under contract with the National Aeronautics and Space Administration.

This research has made use of the VizieR catalog access tool, CDS, Strasbourg, France.

Software: Astropy (Astropy Collaboration et al. 2013; Price-Whelan et al. 2018), matplotlib (Hunter 2007), SciPy (Virtanen et al. 2020), the IPython package (Pérez & Granger 2007), NumPy (Van Der Walt et al. 2011), pandas (McKinney 2010, 2011), Astroquery (Ginsburg et al. 2019), extinction (Barbary 2021).

Appendix A
Fitting Gallery

Here, we include an abbreviated gallery of fitting results for the NSA (Figure 13) and UDG samples (Figure 14).

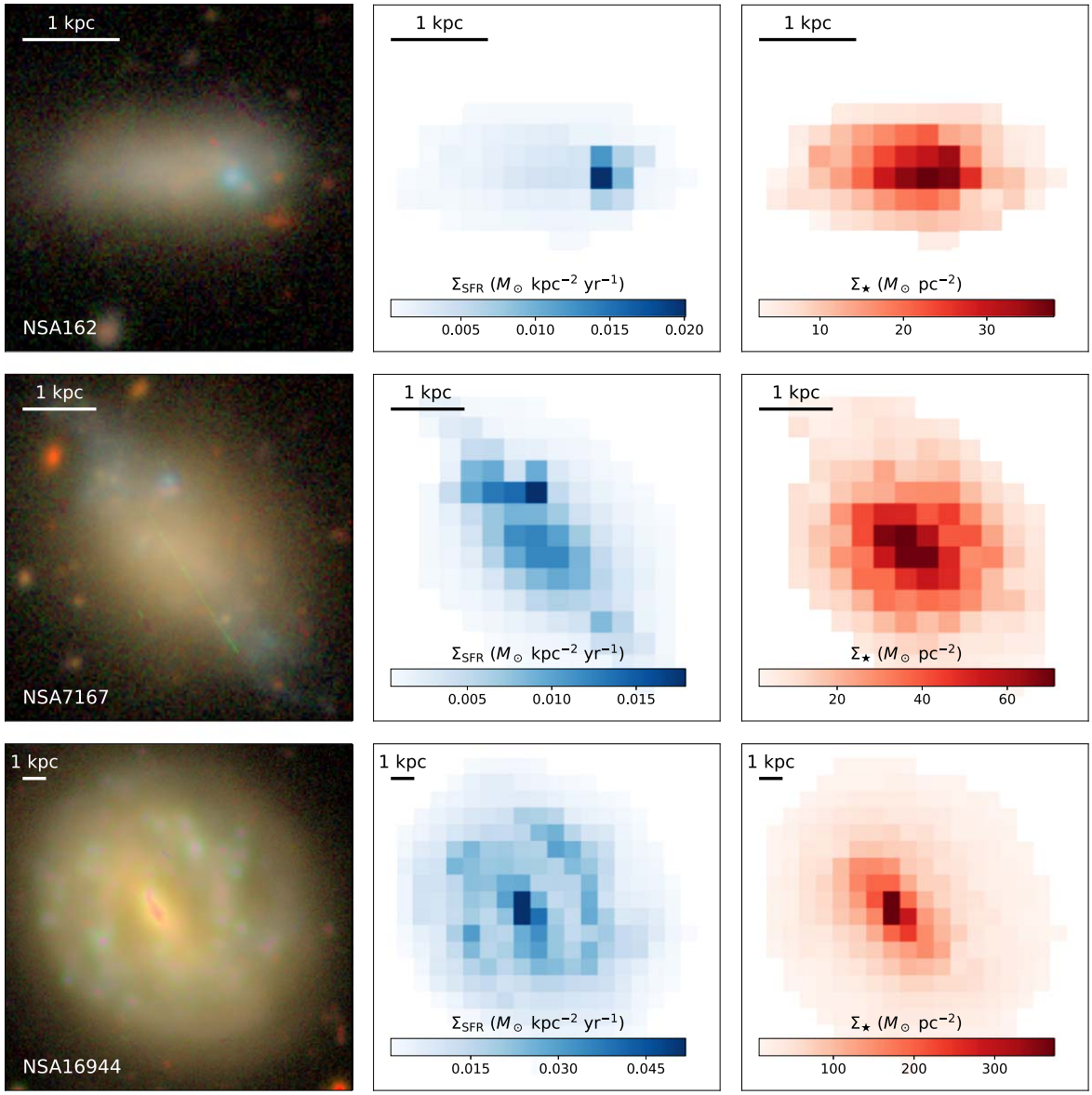

Figure 13. A sample of three example galaxies from the NSA sample, as labeled. From the left, we show the HSC-SSP gri-composite RGB image, the median SFR surface density map, and the median stellar mass surface density map. These galaxies are chosen to span the range of morphologies present in the sample.

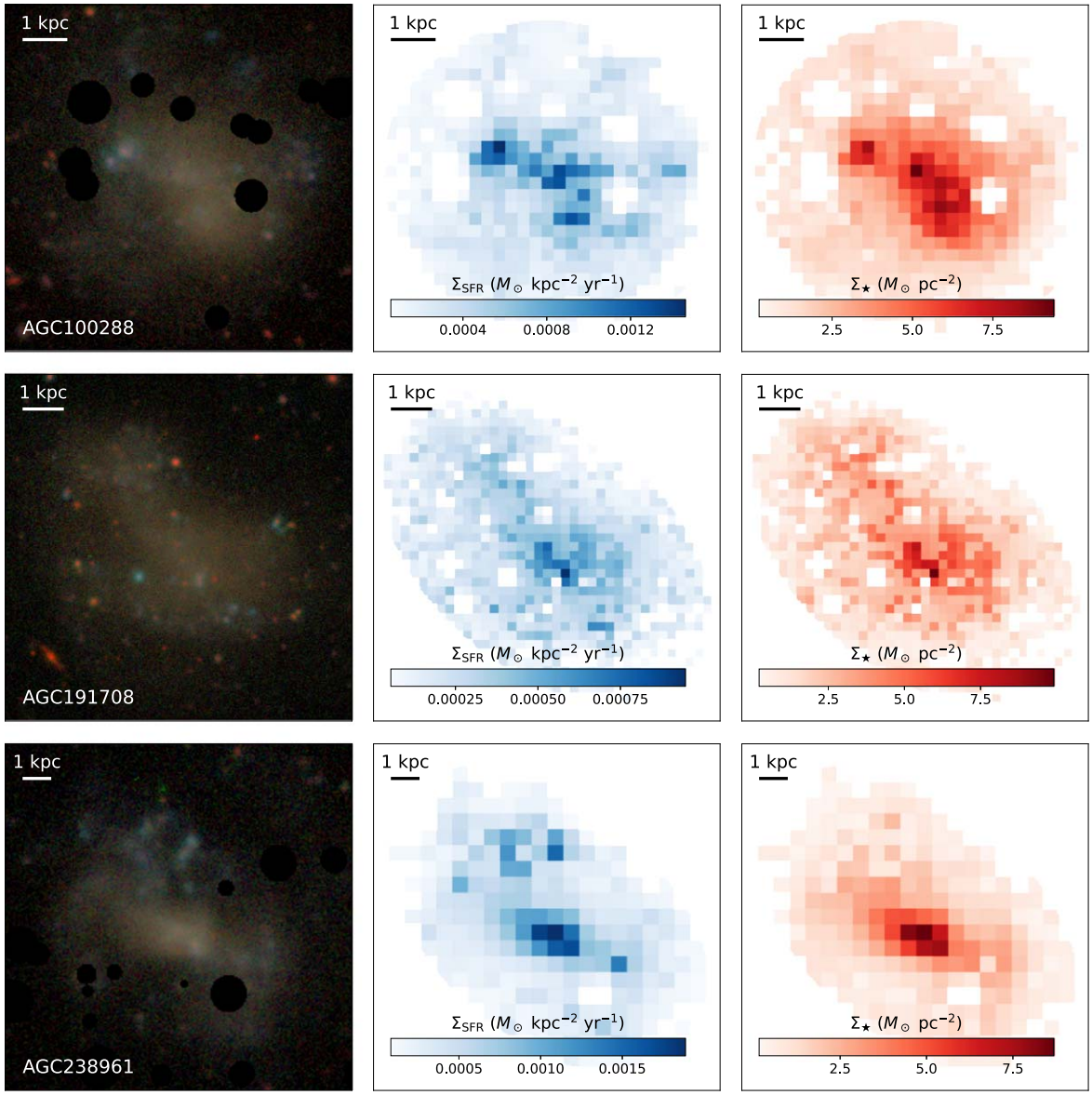

Figure 14. A sample of three example galaxies from the UDG sample, as labeled. From the left, we show the HSC-SSP gri-composite RGB image, the median SFR surface density map, and the median stellar mass surface density map. These galaxies are chosen to span the range of morphologies present in the sample.

Appendix B
Additional Validation of the SED Fitting

Due to the novelty of our joint fitting approach, we describe three additional validation steps here. First, we show a typical corner plot for one of the jointly fitted SEDs (the example shows NSA 7167) in Figure 15. We find that the inferred parameters are strongly peaked and unimodal, though there is a degeneracy between the age and amplitude (stellar mass) inferred for each cluster SED. This is a physically expected effect since an increase in age leads to a drop in the mass-to-light ratio of the stellar population, meaning that more stellar mass is necessary to achieve the same luminosity. We find no significant degeneracy between parameters inferred for different cluster SEDs.

Next, we show in Figure 16 a comparison between the SED fitting results using the global optical photometry and those derived using the cluster SEDs. We find no evidence for a systematic shift between the global and joint fitting methods. Indeed, the total stellar mass and SFR inferred via the joint fit method are in good agreement with those estimated via the global fit method, as shown by the text in each panel.

Finally, as stated in the main text, we assume a fixed metallicity in the SED fitting presented in this paper. There is some evidence that low surface brightness galaxies may have higher than average gas-phase metallicities (Greco et al. 2018a; Sánchez Almeida et al. 2018), though we caution that these results contain only three low surface brightness galaxies, and that these low surface brightness galaxies are an optically selected sample (as opposed to the H I-selected UDGs in the sample discussed in this work). We find that assuming solar metallicity models shifts the total SFR and stellar mass estimates by less than 0.1 dex compared to the fiducial estimates, as shown in Figure 17. The stellar masses estimated using solar metallicity models are slightly lower (with a median difference between solar metallicity and fiducial values of −0.08 dex), and the SFRs are slightly higher (with a median difference of 0.09 dex). This shift is expected—the higher metallicity models are redder at fixed age, meaning that the

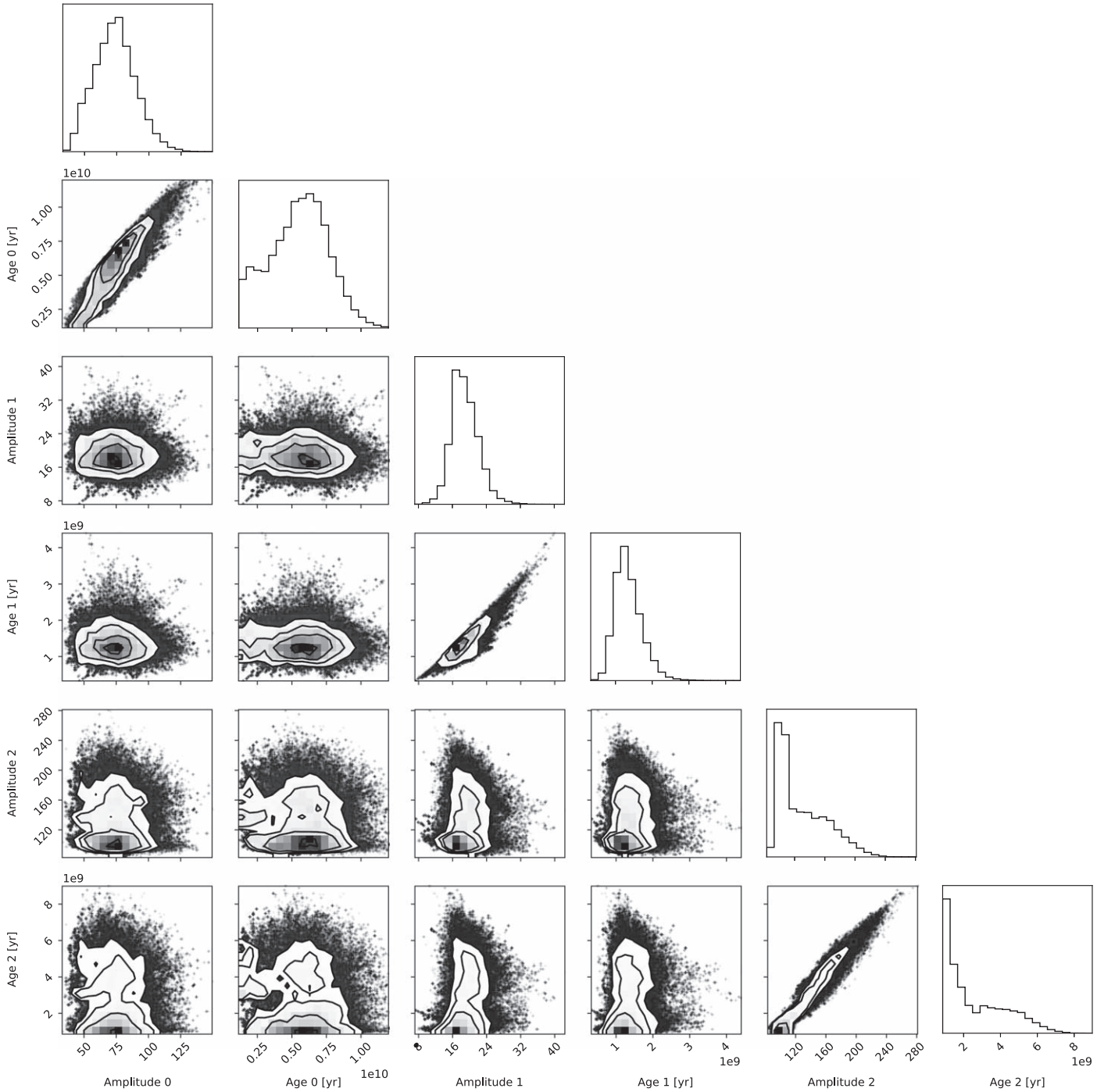

Figure 15. A corner plot of the parameter inference for NSA 7167. As expected, although the 1D distribution of the parameters are strongly peaked and unimodal, there is some degeneracy in the tails of the distribution between the age and amplitude of each component. This can be understood naturally by considering that as the age of a component increases, the mass-to-light ratio drops, meaning that the amplitude of that component (i.e., the stellar mass) must increase to account for the same luminosity.

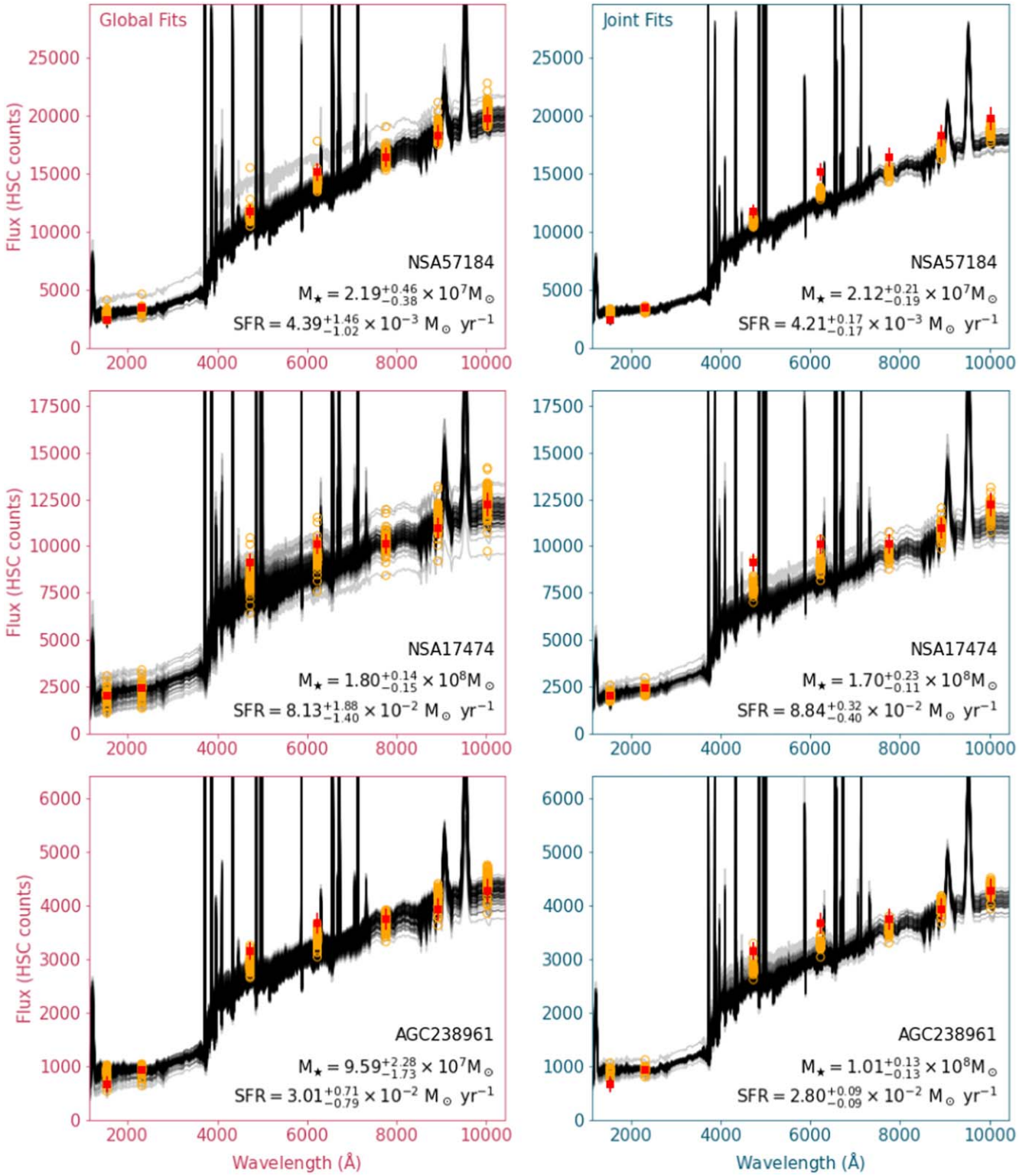

Figure 16. A comparison of the global SED fits (left column) and joint SED fits (right column) for three galaxies in our sample. In each panel, the red points show the observed fluxes in FUV, NUV, g_{HSC}, r_{HSC}, i_{HSC}, z_{HSC}, and y_{HSC}. Each black curve and set of orange points show the spectrum and synthetic photometry, respectively, of one drawn from the posterior. The text shows the median stellar mass and SFR estimates for each fit; uncertainties correspond to the 16th and 84th percentiles of the posterior.

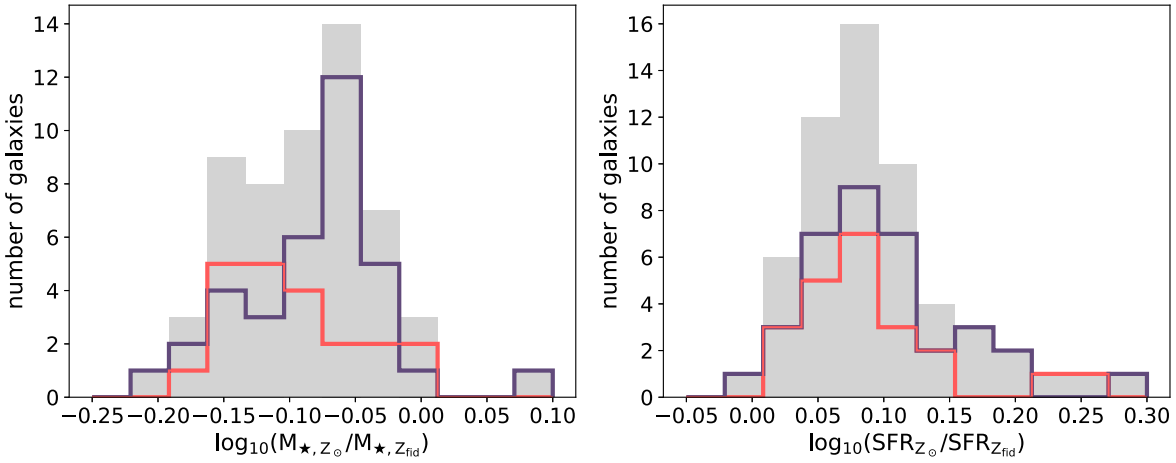

Figure 17. A comparison between the total stellar mass (left) and SFR (right) estimates derived from our spatially resolved SED fitting if we assume a metallicity of $Z = 0.012$ (as opposed to our fiducial value of $Z = 0.004$). In both panels, the gray-filled histogram shows the distribution over all galaxies—the unfilled red and purple histograms show the distribution over the UDG and NSA samples, respectively.

best-fit stellar populations will be on average slightly younger at fixed color.

Appendix C
H I Profile Recovery

Although the subset of the Janowiecki et al. (2019) UDGs with resolved H I observations from Gault et al. (2021) are disjoint from the subset of Janowiecki et al. (2019) UDGs in this work, we can do a simple test of our H I profile recovery alone using the Gault et al. (2021) galaxies.

In Figure 18 we show a comparison between the H I profiles estimated from the Gault et al. (2021) structural measurements (dashed curves) with profile estimates analogous to those presented in the main body of this work (solid curve and filled region). We also show the directly measured profiles of Leroy et al. (2008) as solid gray curves in each panel. We find that the profiles are generally well recovered in the range of $\Sigma_{\rm H\ I}$ probed by the Leroy et al. (2008) sample. We do find that the inferred Gault et al. (2021) profiles with very high H I surface densities (AGC 749251, $\Sigma_{\rm H\ I} \gtrsim 30\ M_\odot\ {\rm pc}^{-2}$) are significantly underestimated. However, we caution that the Gault et al. (2021) profiles are estimated from their measured H I masses, isophotal sizes, and fraction of H I contained within that isophotal size—not directly measured profiles. We also note that it is expected theoretically that the maximum H I surface density of these systems should be $\sim 10\ M_\odot\ {\rm pc}^{-2}$ on kiloparsec scales (Krumholz 2013).

We thus find that our average H I profile estimation technique works well to capture the average behavior of the Gault et al. (2021) resolved UDG measurements, though we caution that this test is quite limited in scope due to the inclusion of the Gault et al. (2021) inferred profiles in creating the profile estimation method. As expected, the average estimation method performs better for galaxies with average H I surface densities than for UDGs with notably high or low H I surface densities. Because our analysis focuses on the bulk

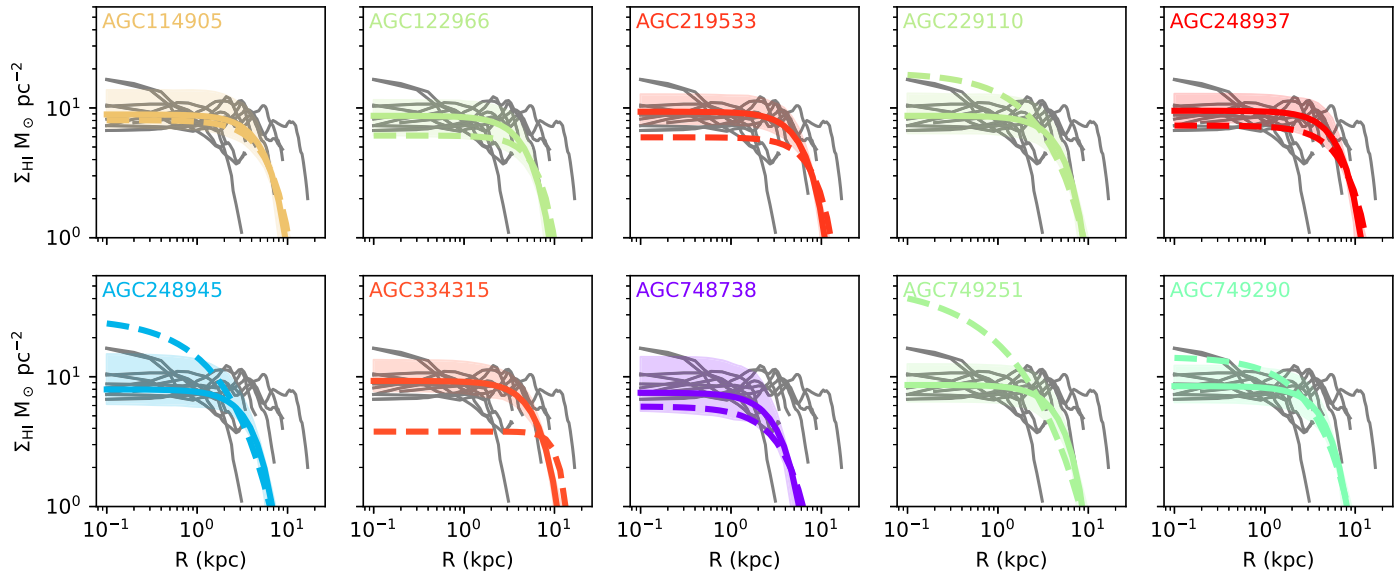

Figure 18. In each panel, we show the H I radial profile inferred from the Gault et al. (2021) reported structural parameters as a dashed curve and our estimated radial profile as a solid curve. We also show the directly measured profiles of Leroy et al. (2008) as gray curves in each panel. We find that our estimation method adequately recovers the UDG inferred radial H I profiles, with significantly better performance for inferred profiles close to the average profile—an unsurprising result given that we estimate profiles by assigning galaxies' average Sérsic parameters for their H I mass.

behavior of the dwarfs in our sample as opposed to the properties of individual galaxies (and because high-resolution H I data are not yet available for sufficiently large samples of UDGs), we find in this limited test case that our estimation method is well suited for the purpose of this work.

ORCID iDs

Erin Kado-Fong https://orcid.org/0000-0002-0332-177X
Jenny E. Greene https://orcid.org/0000-0002-5612-3427
Song Huang https://orcid.org/0000-0003-1385-7591
Andy Goulding https://orcid.org/0000-0003-4700-663X

References

Aihara, H., AlSayyad, Y., Ando, M., et al. 2019, PASJ, 71, 114
Amorisco, N. C., & Loeb, A. 2016, MNRAS, 459, L51
Astropy Collaboration, Robitaille, T. P., Tollerud, E. J., et al. 2013, A&A, 558, A33
Barbary, K. 2021, extinction: Dust extinction laws, Astrophysics Source Code Library, ascl:2102.026
Beasley, M. A., & Trujillo, I. 2016, ApJ, 830, 23
Bell, E. F., McIntosh, D. H., Katz, N., & Weinberg, M. D. 2003, ApJS, 149, 289
Bellstedt, S., Robotham, A. S. G., Driver, S. P., et al. 2021, MNRAS, 503, 3309
Berg, D. A., Skillman, E. D., Marble, A. R., et al. 2012, ApJ, 754, 98
Bertin, E., & Arnouts, S. 1996, A&AS, 117, 393
Bradford, J. D., Geha, M. C., & Blanton, M. R. 2015, ApJ, 809, 146
Brinchmann, J., Charlot, S., White, S. D. M., et al. 2004, MNRAS, 351, 1151
Calzetti, D. 2013, in Secular Evolution of Galaxies, ed. J. Falcón-Barroso & J. H. Knapen (Cambridge: Cambridge Univ. Press), 419
Carnall, A. C., Leja, J., Johnson, B. D., et al. 2019, ApJ, 873, 44
Chan, T. K., Kereš, D., Wetzel, A., et al. 2018, MNRAS, 478, 906
Conroy, C., & Gunn, J. E. 2010, ApJ, 712, 833
Conroy, C., Gunn, J. E., & White, M. 2009, ApJ, 699, 486
Dalcanton, J. J., Spergel, D. N., Gunn, J. E., Schmidt, M., & Schneider, D. P. 1997, AJ, 114, 635
Danieli, S., van Dokkum, P., Conroy, C., Abraham, R., & Romanowsky, A. J. 2019, ApJL, 874, L12
Danieli, S., van Dokkum, P., Trujillo-Gomez, S., et al. 2021, ApJL, 927, L28
de los Reyes, M. A. C., & Kennicutt, R. C. J. 2019, ApJ, 872, 16
Di Cintio, A., Brook, C. B., Dutton, A. A., et al. 2017, MNRAS, 466, L1
Di Cintio, A., Brook, C. B., Macciò, A. V., Dutton, A. A., & Cardona-Barrero, S. 2019, MNRAS, 486, 2535
Greene, J., Greco, J. P., Goulding, A. D., et al. 2022, ApJ, 933, 150
El-Badry, K., Wetzel, A., Geha, M., et al. 2016, ApJ, 820, 131
Foreman-Mackey, D., Hogg, D. W., Lang, D., & Goodman, J. 2013, PASP, 125, 306
Gault, L., Leisman, L., Adams, E. A. K., et al. 2021, ApJ, 909, 19
Ginsburg, A., Sipőcz, B. M., Brasseur, C. E., et al. 2019, AJ, 157, 98
Greco, J. P., Goulding, A. D., Greene, J. E., et al. 2018a, ApJ, 866, 112
Greco, J. P., Greene, J. E., Strauss, M. A., et al. 2018b, ApJ, 857, 104
Haynes, M. P., Giovanelli, R., Martin, A. M., et al. 2011, AJ, 142, 170
Hopkins, P. F., Kereš, D., Oñorbe, J., et al. 2014, MNRAS, 445, 581
Hopkins, P. F., Wetzel, A., Kereš, D., et al. 2018, MNRAS, 480, 800
Huang, S., Leauthaud, A., Greene, J. E., et al. 2018, MNRAS, 475, 3348
Hunter, D. A., Elmegreen, B. G., Goldberger, E., et al. 2021, AJ, 161, 71
Hunter, J. D. 2007, CSE, 9, 90
Into, T., & Portinari, L. 2013, MNRAS, 430, 2715
IRSA 2022, Galactic Dust Reddening and Extinction, IPAC doi:10.26131/IRSA537
Janowiecki, S., Jones, M. G., Leisman, L., & Webb, A. 2019, MNRAS, 490, 566
Jiang, F., Dekel, A., Freundlich, J., et al. 2019, MNRAS, 487, 5272
Jimmy, Tran, K.-V., Saintonge, A., et al. 2015, ApJ, 812, 98
Kado-Fong, E., Greene, J. E., Huang, S., et al. 2020, ApJ, 900, 163
Kado-Fong, E., Greene, J. E., Kim, C.-G., & Lancaster, L. 2022, ApJ, 939, 101
Kado-Fong, E., Petrescu, M., Mohammad, M., et al. 2021, ApJ, 920, 72
Karachentsev, I. D., Kaisina, E. I., & Kaisin, S. S. 2021, MNRAS, 506, 1346
Karunakaran, A., Spekkens, K., Zaritsky, D., et al. 2020, ApJ, 902, 39
Kauffmann, G., Heckman, T. M., White, S. D. M., et al. 2003, MNRAS, 341, 33
Kennicutt, R. C. J. 1989, ApJ, 344, 685
Kennicutt, R. C. J. 1998, ARA&A, 36, 189
Kim, C.-G., Kim, W.-T., & Ostriker, E. C. 2011, ApJ, 743, 25
Kim, C.-G., & Ostriker, E. C. 2015, ApJ, 815, 67
Kim, C.-G., Ostriker, E. C., & Kim, W.-T. 2013, ApJ, 776, 1
Kim, C.-G., Ostriker, E. C., & Raileanu, R. 2017, ApJ, 834, 25
Kroupa, P. 2001, MNRAS, 322, 231
Krumholz, M. R. 2013, MNRAS, 436, 2747
Lee, H., Skillman, E. D., Cannon, J. M., et al. 2006, ApJ, 647, 970
Leisman, L., Haynes, M. P., Janowiecki, S., et al. 2017, ApJ, 842, 133
Leroy, A. K., Walter, F., Brinks, E., et al. 2008, AJ, 136, 2782
Li, J., Huang, S., Leauthaud, A., et al. 2022, MNRAS, 515, 5335
Liao, S., Gao, L., Frenk, C. S., et al. 2019, MNRAS, 490, 5182
Mancera Piña, P. E., Aguerri, J. A. L., Peletier, R. F., et al. 2019a, MNRAS, 485, 1036
Mancera Piña, P. E., Fraternali, F., Adams, E. A. K., et al. 2019b, ApJL, 883, L33
Mancera Piña, P. E., Fraternali, F., Oman, K. A., et al. 2020, MNRAS, 495, 3636
Mancera Piña, P. E., Fraternali, F., Oosterloo, T., et al. 2022, MNRAS, 512, 3230
Marleau, F. R., Habas, R., Poulain, M., et al. 2021, A&A, 654, A105
Martin, D. C., Fanson, J., Schiminovich, D., et al. 2005, ApJL, 619, L1
Martín-Navarro, I., Romanowsky, A. J., Brodie, J. P., et al. 2019, MNRAS, 484, 3425
McGaugh, S. S., Bothun, G. D., & Schombert, J. M. 1995, AJ, 110, 573
McKinney, W. 2010, in Proc. of the 9th Python in Science Conf. (SciPy 2010), 445, ed. S. van der Walt & J. Millman, 51
McKinney, W. 2011, pandas: a Foundational Python Library for Data Analysis and Statistics, https://www.semanticscholar.org/paper/pandas%3A-a-Foundational-Python-Library-for-Data-and-McKinney/1a62eb61b2663f8135347171e30cb9dc0a8931b5#ref
Ostriker, E. C., McKee, C. F., & Leroy, A. K. 2010, ApJ, 721, 975
Ostriker, E. C., & Shetty, R. 2011, ApJ, 731, 41
Peng, E. W., & Lim, S. 2016, ApJL, 822, L31
Pérez, F., & Granger, B. E. 2007, CSE, 9, 21
Price-Whelan, A. M., Sipőcz, B. M., Günther, H. M., et al. 2018, AJ, 156, 123
Rong, Y., Guo, Q., Gao, L., et al. 2017, MNRAS, 470, 4231
Salim, S., Rich, R. M., Charlot, S., et al. 2007, ApJS, 173, 267
Sánchez Almeida, J., Olmo-García, A., Elmegreen, B. G., et al. 2018, ApJ, 869, 40
Sandage, A., & Binggeli, B. 1984, AJ, 89, 919
Schlafly, E. F., & Finkbeiner, D. P. 2011, ApJ, 737, 103
Schmidt, M. 1959, ApJ, 129, 243
Simha, V., Weinberg, D. H., Conroy, C., et al. 2014, arXiv:1404.0402
Trujillo-Gomez, S., Kruijssen, J. M. D., & Reina-Campos, M. 2022, MNRAS, 510, 3356
van der Walt, S., Colbert, S. C., & Varoquaux, G. 2011, CSE, 13, 22
van Dokkum, P., Danieli, S., Cohen, Y., et al. 2018, Natur, 555, 629
van Dokkum, P., Wasserman, A., Danieli, S., et al. 2019, ApJ, 880, 91
van Dokkum, P. G., Abraham, R., Merritt, A., et al. 2015, ApJL, 798, L45
Van Nest, J. D., Munshi, F., Wright, A. C., et al. 2022, ApJ, 926, 92
Villaume, A., Romanowsky, A. J., Brodie, J., et al. 2022, ApJ, 924, 32
Virtanen, P., Gommers, R., Oliphant, T. E., et al. 2020, NatMe, 17, 261
Wang, L., Dutton, A. A., Stinson, G. S., et al. 2015, MNRAS, 454, 83
Wright, A. C., Tremmel, M., Brooks, A. M., et al. 2021, MNRAS, 502, 5370
Yagi, M., Koda, J., Komiyama, Y., & Yamanoi, H. 2016, ApJS, 225, 11
Zaritsky, D., Donnerstein, R., Karunakaran, A., et al. 2022, ApJS, 261, 11